

8-1-2022

Design and Fabrication of an Apparatus for Tao High-Resolution Laser Spectroscopy

Timothy Chung

Follow this and additional works at: <https://digitalscholarship.unlv.edu/thesesdissertations>



Part of the [Physics Commons](#)

Repository Citation

Chung, Timothy, "Design and Fabrication of an Apparatus for Tao High-Resolution Laser Spectroscopy" (2022). *UNLV Theses, Dissertations, Professional Papers, and Capstones*. 4497.
<http://dx.doi.org/10.34917/33690267>

This Thesis is protected by copyright and/or related rights. It has been brought to you by Digital Scholarship@UNLV with permission from the rights-holder(s). You are free to use this Thesis in any way that is permitted by the copyright and related rights legislation that applies to your use. For other uses you need to obtain permission from the rights-holder(s) directly, unless additional rights are indicated by a Creative Commons license in the record and/or on the work itself.

This Thesis has been accepted for inclusion in UNLV Theses, Dissertations, Professional Papers, and Capstones by an authorized administrator of Digital Scholarship@UNLV. For more information, please contact digitalscholarship@unlv.edu.

DESIGN AND FABRICATION OF AN APPARATUS FOR TAO
HIGH-RESOLUTION LASER SPECTROSCOPY

By

Timothy Chung

Bachelor of Arts – Physics
Occidental College
2017

A thesis submitted in partial fulfillment
of the requirements for the

Master of Science – Physics

Department of Physics & Astronomy
College of Sciences
The Graduate College

University of Nevada, Las Vegas
August 2022



Thesis Approval

The Graduate College
The University of Nevada, Las Vegas

July 7, 2022

This thesis prepared by

Timothy Chung

entitled

Design and Fabrication of an Apparatus for Tao High-Resolution Laser Spectroscopy

is approved in partial fulfillment of the requirements for the degree of

Master of Science – Physics
Department of Physics & Astronomy

Yan Zhou, Ph.D.
Examination Committee Chair

Joshua Island, Ph.D.
Examination Committee Member

Bernard Zygelman, Ph.D.
Examination Committee Member

Balakrishnan Naduvalath, Ph.D.
Graduate College Faculty Representative

Alyssa Crittenden, Ph.D.
*Vice Provost for Graduate Education &
Dean of the Graduate College*

ABSTRACT

In this study, an apparatus for the high-resolution laser spectroscopy of molecules is designed and constructed. The apparatus is used to identify TaO transitions, but may be used for any other molecular species in the future. It will also later be used for experiments such as quantum logic spectroscopy, which are enabled by attachable chambers that can be supplied with molecules from the apparatus. Several considerations are made to improve the quality and longevity of the apparatus such as regulating the rovibrational states of the produced molecules, optimizing the linewidth of the ionization lasers, reducing noise from sources such as laser scattering, creating interlocks, and more. As a final test, we check for Ta and TaO signals at known transitions. A rough scan through the wavelength range of 615.6 - 629.8 nm and its frequency doubled counterpart yields peaks for Ta that correspond to 310.4150 and 312.8772 nm from the NIST Atomic Spectra Database. Two peaks for TaO agree with ν_{00} transitions from the ground to E (15880.6 cm^{-1}) and F 10 (16051 cm^{-1}) states found in the NIST Chemistry WebBook, while a third peak is likely associated with the ν_{11} transition from the ground to F 10 state. Our scan shows good agreement, and so the next step is to improve the scan resolution to study the spectrum in more detail.

TABLE OF CONTENTS

ABSTRACT	iii
LIST OF FIGURES	vi
CHAPTER 1 INTRODUCTION	1
eEDM and NMQM measurements	1
TaO ⁺	4
REMPI	7
CHAPTER 2 DESCRIPTION OF APPARATUS	9
Apparatus overview	9
Assembly and machining	11
Picomotor control	13
Supersonic jet nozzle	14
Ta rod ablation	20
Vacuum system	26
Spectroscopic laser system	28
Dye laser wavelength characterization	36
Timing system	46
CHAPTER 3 EXPERIMENTAL RESULTS	48
Optimizations	48
Ta and TaO	49
CHAPTER 4 OUTLOOK	53
BIBLIOGRAPHY	55
CURRICULUM VITAE	57

LIST OF FIGURES

1.1	Motivations of eEDM and NMQM measurements in the scope of testing fundamental CP-violation.	2
1.2	Constraints on the eEDM given by JILA [1] and ACME [2].	3
1.3	Ground state configuration of TaO^+	4
1.4	Measurement schemes of eEDM and NMQM using trapped TaO^+ molecular ions. Left image shows hyperfine structures of $^{181}\text{TaO}^+$, $^3\Delta_1$, $v^+=0$, $J^+=1$, $I^+=7/2$ without applied electric or magnetic fields. Right image shows the hyperfine structure at $F=5/2$ with Zeeman and Stark shifts.	5
2.1	Apparatus overview. Source chamber (right) and LIF chamber (left). .	9
2.2	Apparatus supported by a custom built T-slot aluminum frame.	10
2.3	Schematic of clamp used to hold the picomotor.	11
2.4	Schematic of clamp used to support and prevent rotation of the high pressure cell assembly.	11
2.5	Cross-section view of the high pressure cell and PZT assembly. The gas mixture is introduced from above, and the source chamber is located below.	14
2.6	Circuit diagram of negative HV pulser for the PZT.	16
2.7	Voltage change without PZT.	18
2.8	Voltage change with PZT.	18
2.9	Cross section view of supersonic jet nozzle.	20
2.10	Optical setup for adjusting focal point of ablation laser. Focal point of lenses: a=-25 mm, b=125 mm, c=-100 mm, d=100 mm. e shows the focal point of the ablation laser in perspective with the supersonic jet nozzle.	20
2.11	Schematic of high pressure cell assembly. (Move this figure to the laser ablation part)	21
2.12	Cross section of parabolic mirror assembly situated in LIF chamber. ..	22
2.13	Cross section of parabolic mirror assembly situated in LIF chamber. ..	23
2.14	PMT switch circuit designed by JILA Electronics Lab.	25
2.15	Inner structure of a turbo pump. Reprinted from Wikimedia Commons.	26
2.16	Diagram of baking system.	28
2.17	Optical configuration of the dye laser [3].	30
2.18	Diagram showing the mth order diffraction of the grating.	31

2.19	Diagram showing the path difference between adjacent reflected beams.	
	32	
2.20	Diagram showing the diffraction orders of a 624 nm laser.....	32
2.21	Non-linear optical crystal for frequency doubling and a compensator to correct the beam path [3].	34
2.22	Trajectory of dye laser and its second harmonic in a Pellin-Broka prism arrangement.	35
2.23	Diagram showing the orientation of the ASE and laser beam. The grey region is the area exposed to the Nd:YAG laser, which is passed through a cylindrical lens. The parasitic oscillation arises between the dye cell walls [3].	35
2.24	Path of laser going through the monitor etalon. Constructive interference may occur at multiple angles bounded by the path of the laser. ..	37
2.25	Interference fringes for 624.5588 nm (a), 624.5625 nm (b), 624.5662 nm (c), 624.5700 nm (d), 624.5740 nm (e), and 624.5779 nm (f). Spacing between fringes is nonlinear but corresponds to the same resonance frequency.	40
2.26	Left: Vertical slice across the center of interference fringes. Position is in pixels and intensity is the sum of RGB values. Right: x scale has a correction to the non-linearity so that peaks are equidistant.	41
2.27	Comparison of peak position vs peak enumeration for the original data and a function obtained from curve fitting. Peak position is taken as the distance in pixels from the center of the interference fringes.	41
2.28	Closer view of the first two peaks to the right of the center. Peak widths are obtained through Gaussian fits.	43
2.29	Wavemeter comparison between a) dye laser and b) a single mode 780 nm laser. Upper and lower plots correspond to low and high-resolution Fizeau wedges respectively [4]. Horizontal axis represents the position of the interference signal (arb. units) and vertical axis is the relative intensity of the signal (arb. units).	44
2.30	Timing of pulses in pulse generator for TaO.....	47
3.1	Photodetector readings without oxygen.	49
3.2	Photodetector readings with oxygen.	50
3.3	Photodetector readings with oxygen over a wider frequency range.	51

CHAPTER 1

INTRODUCTION

eEDM and NMQM measurements

To our best understanding, the universe contains more matter than antimatter. Back in 1968, Soviet physicist Andrei Sakharov stated three conditions for the evolution of a matter-dominated universe from one that starts with equal amounts of matter and antimatter. First, that baryon-violating interactions exist; second, that the universe is out of thermal equilibrium; and third, that there is enough Charge (C) and Charge-Parity (CP) symmetry violation [5]. The first two conditions are accounted for in the Standard Model of particle physics. As for the last condition, there is enough C symmetry violation, but insufficient amounts of CP violation, and only in weak interactions.

Symmetry violation can be explained with the electron as an example, shown in the bottom of Figure 1.2. If the electron has an electron electric dipole moment (eEDM), applying the time-reversal operator flips the spin and not the dipole. This can be seen in the sense that going backwards in time reverses the direction of the angular momentum, but doesn't affect the physical orientation of the electron. Likewise, parity symmetry is violated when the dipole flips, but not the spin, such as in a mirror image of the electron [6]. For now, CPT invariance is a consistent phenomenon for

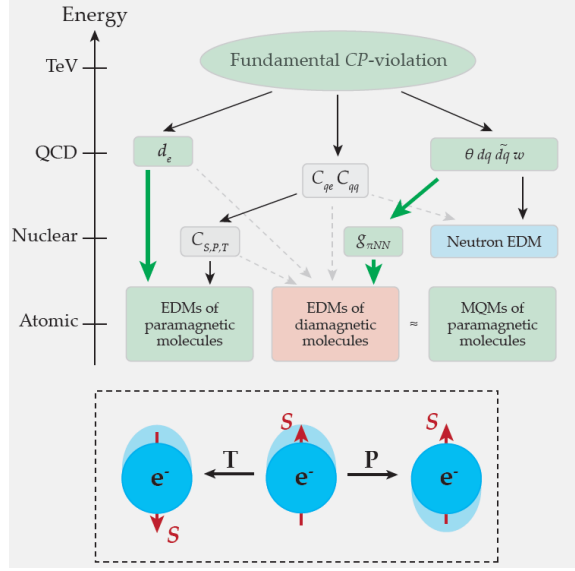


Figure 1.1: Motivations of eEDM and NMQM measurements in the scope of testing fundamental CP-violation.

which no violation has been observed. Conservation of CPT symmetry implies that CP violations have an associated T violation and vice versa.

The standard model predicts the eEDM to be on the order of 10^{-38} e cm, which is far below current experimental sensitivities [7]. There are also extensions to the standard model that predict new particles and interactions which could break CP symmetry, but generally require the eEDM to fall roughly between 10^{-27} and 10^{-30} e cm [2].

The minimum upper bound of the eEDM is currently found to be at 1.1×10^{-29} e cm, which rules out some of the extension theories [2]. Further reducing this upper bound could help narrow down the list of possible new particles that could exist.

The nuclear EDM, either from diamagnetic atoms or neutrons, could also reveal CP(T) violation by different mechanisms. However, neutron EDM is not a table-top

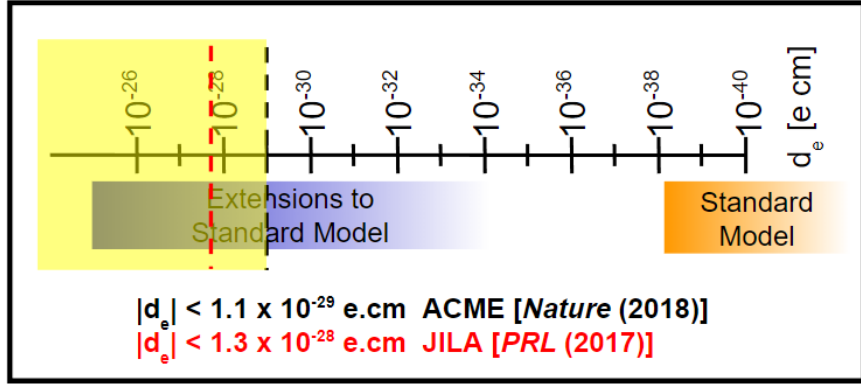


Figure 1.2: Constraints on the eEDM given by JILA [1] and ACME [2].

AMO physics experiment, and the atomic EDM is shielded almost completely by electrons. Theorists propose to use higher order nuclear moments instead, such as the nuclear magnetic quadrupole moment (NMQM) [8]. As electrons are significantly less effective at shielding magnetic fields, this higher order interaction could be more sensitive to the fundamental physics than the EDM. Paramagnetic molecules such as TaO provide the capability for both eEDM and NMQM measurements [9].



TaO^+ is an appealing molecular ion not only for its sensitivity to the eEDM and NMQM, but also for its stability, simplicity, and ground state configuration [10]. It has a large effective E-field, characteristic of paramagnetic molecules, which is used in determining the eEDM. The net nuclear spin of the Ta atom is 7/2 which, later discussed in more detail, allows for measurement of the NMQM. Additionally, the net nuclear spin of the O atom is 0, simplifying the hyperfine structure.

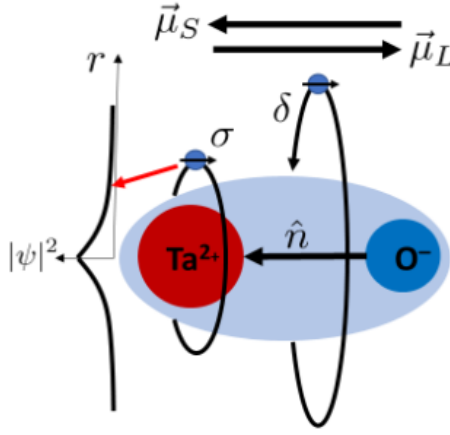


Figure 1.3: Ground state configuration of TaO^+

The ground state of TaO^+ is predicted to be the $^3\Delta_1$ state [10]. This corresponds to a total spin quantum number S of 1, projection of the orbital angular momentum along the internuclear axis Λ of ± 2 , and projection of the total angular momentum along the internuclear axis Ω of 1. This state has two valence electrons, σ and δ . The δ electron can orientate the molecule when exposed to a small external electric field, in turn generating a large internal effective electric field near the heavy metal atom.

The σ electron is located very near to this heavy atom and senses the large effective electric field. Additionally, the contributions from electron spin and orbital angular momentum cancel out, resulting in a near zero magnetic g-factor. This small g-factor suppresses many systematics from the drifting external magnetic field [11].

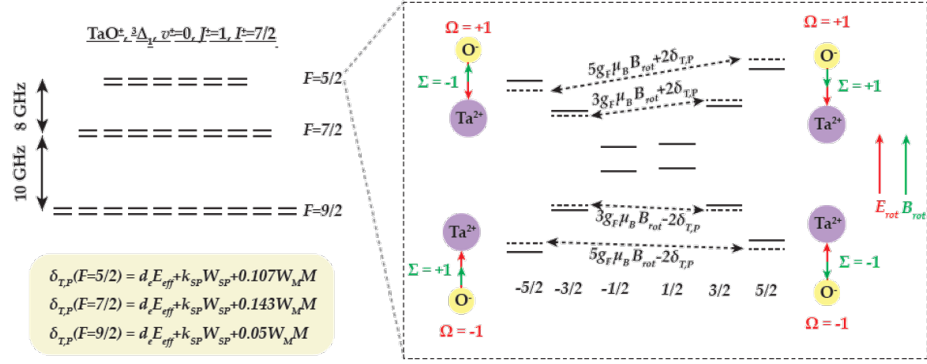


Figure 1.4: Measurement schemes of eEDM and NMQM using trapped TaO^+ molecular ions. Left image shows hyperfine structures of $^{181}\text{TaO}^+$, $^3\Delta_1$, $v^+=0$, $J^+=1$, $I^+=7/2$ without applied electric or magnetic fields. Right image shows the hyperfine structure at $F=5/2$ with Zeeman and Stark shifts.

Figure 1.4 shows the hyperfine structure of TaO^+ with and without E and B fields. For each group of hyperfine states with a specific F quantum number, there are $2(2F+1)$ magnetic sub-levels with Ω -doubling structures of opposite parities, where the upper and lower levels correspond to $\Omega = +1, -1$ respectively. The right side of Figure 1.4 shows the quantum states of $F=5/2$, with applied electric and magnetic fields, as solid lines. The dashed lines represent state shifts induced by T,P-odd interactions. The dashed arrows correspond to actual frequency measurements, which contain information of both regular electron spin resonance and T,P-odd interactions.

The latter can be extracted from a linear combination of at least two such frequency measurements. To separate T,P-odd interactions in the leptonic sector (eEDM and electron-nucleon SPS interaction) from those in the hadronic sector (NMQM), measurements have to be performed in different hyperfine states. For each group of hyperfine states, eEDM and electron-nucleon SPS interactions are identical, but the NMQM interactions are different, as described by equations shown in Figure 1.4, where M is the NMQM, k_{SP} , and W_M are parameters connecting T,P-odd effects to actual frequency shifts. These parameters are obtained from molecular electronic structure calculations [10].

The $^3\Delta_1$ state of TaO^+ , with a rotational state $J=1$ and net nuclear spin $I=7/2$, yields three different values for the total angular momentum F . Applying a parallel E and B field will induce shifts in the hyperfine structure, some of which may exhibit T or P violation [10].

The previously discussed method is used to obtain the eEDM. However, now the difference is attributed not only to the eEDM, but also to nucleus-electron interactions and the NMQM, the latter denoted by M . Different hyperfine states have different sensitivities of eEDM and NMQM. The numerical coefficients for the NMQM are derived from angular momentum coupling calculations.

The eEDM can be separated from the NMQM by two sets of measurements at different hyperfine states. Additionally, different measurements at the same hyperfine states can be applied to check and reduce systematics.

REMPI

The discussion so far has been on the hyperfine structure of TaO^+ for vibrational state $v=0$ and rotational state $J=1$. Changing J will also change F , which can significantly alter the hyperfine structure or completely change the measurement scheme. Different values of v may also affect the hyperfine structure but to a lesser degree. However, the vibrational excited state has a much shorter lifetime that is incompatible for precision measurements. Therefore, producing ions at $v=0$, $J=1$ state is required. We use resonance-enhanced multiphoton ionization (REMPI), which is a technique commonly used in spectroscopy. REMPI of a supersonic cooled molecular beam has been shown to be able to prepare molecular ions that are in a single electronic and vibrational state, and distributed in a few rotational states.

REMPI is a multistage ionization process, using an intermediate excitation state with a narrow linewidth to obtain a population with a well-defined rotation and vibration state, then ionizing from that intermediate state. In comparison, a single ionization laser could ionize the entire population, which could already have a variety of different rotational states, doing little to reduce the number of rotational states. A supersonic beam helps by producing a population with a few rotation and one or two vibration states prior to REMPI. TaO molecules produced in this beam, through ablating a Ta rod and having Ta particles react with O_2 , have ≈ 1 K rotational temperature after supersonic expansion, which means most of the population is allocated to few of the lowest rotational states. Most molecules ($\approx 80\%$) are also shown to be produced in the ground vibrational state.

Identification of an appropriate intermediate state is critical to determine the frequency of the lasers used for excitation. In a future study, a survey Laser Induced Fluorescence (LIF) spectroscopy will be performed to explore the unexplored regime of 30,000-45,000 wavenumber (cm^{-1}) for such states. The capability to ionize molecular species will be important for additional studies using this apparatus, such as quantum logic spectroscopy.

CHAPTER 2

DESCRIPTION OF APPARATUS

Apparatus overview

The apparatus consists of two vacuum chambers as shown in Figure 2.1. Each chamber is connected to a turbo pump, which provides a vacuum of 10^{-5} torr for the source chamber (right) and high vacuum 10^{-7} torr for the LIF chamber (left).

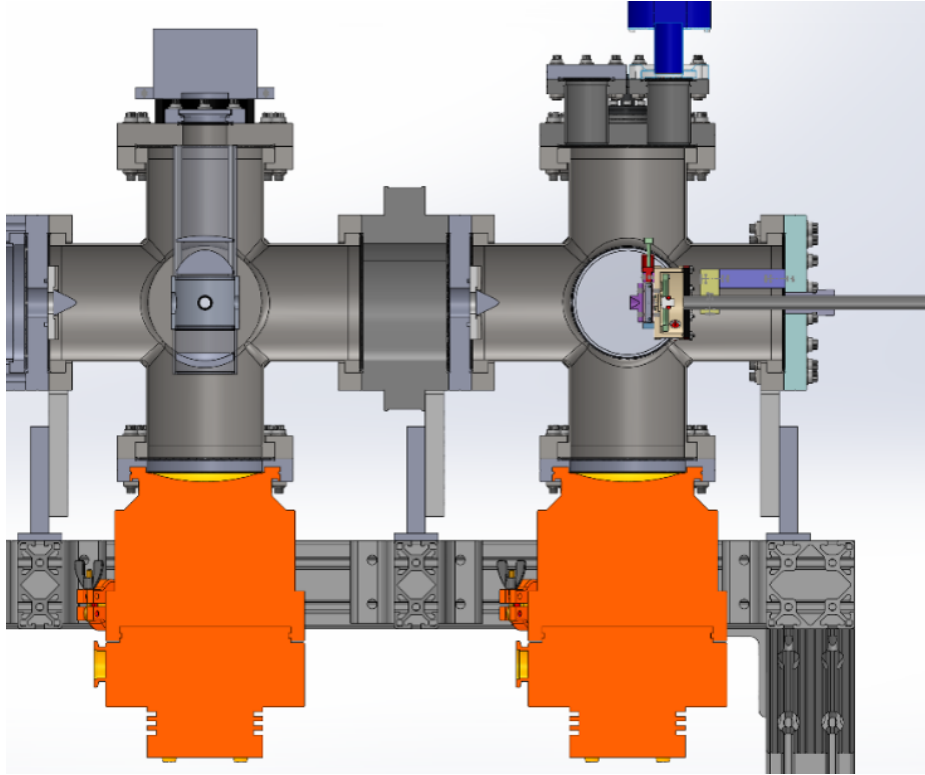


Figure 2.1: Apparatus overview. Source chamber (right) and LIF chamber (left).

The source chamber contains the supersonic beam source where formation of TaO through laser ablation also takes place. The supersonic beam travels into the LIF chamber, where LIF spectroscopy takes place.

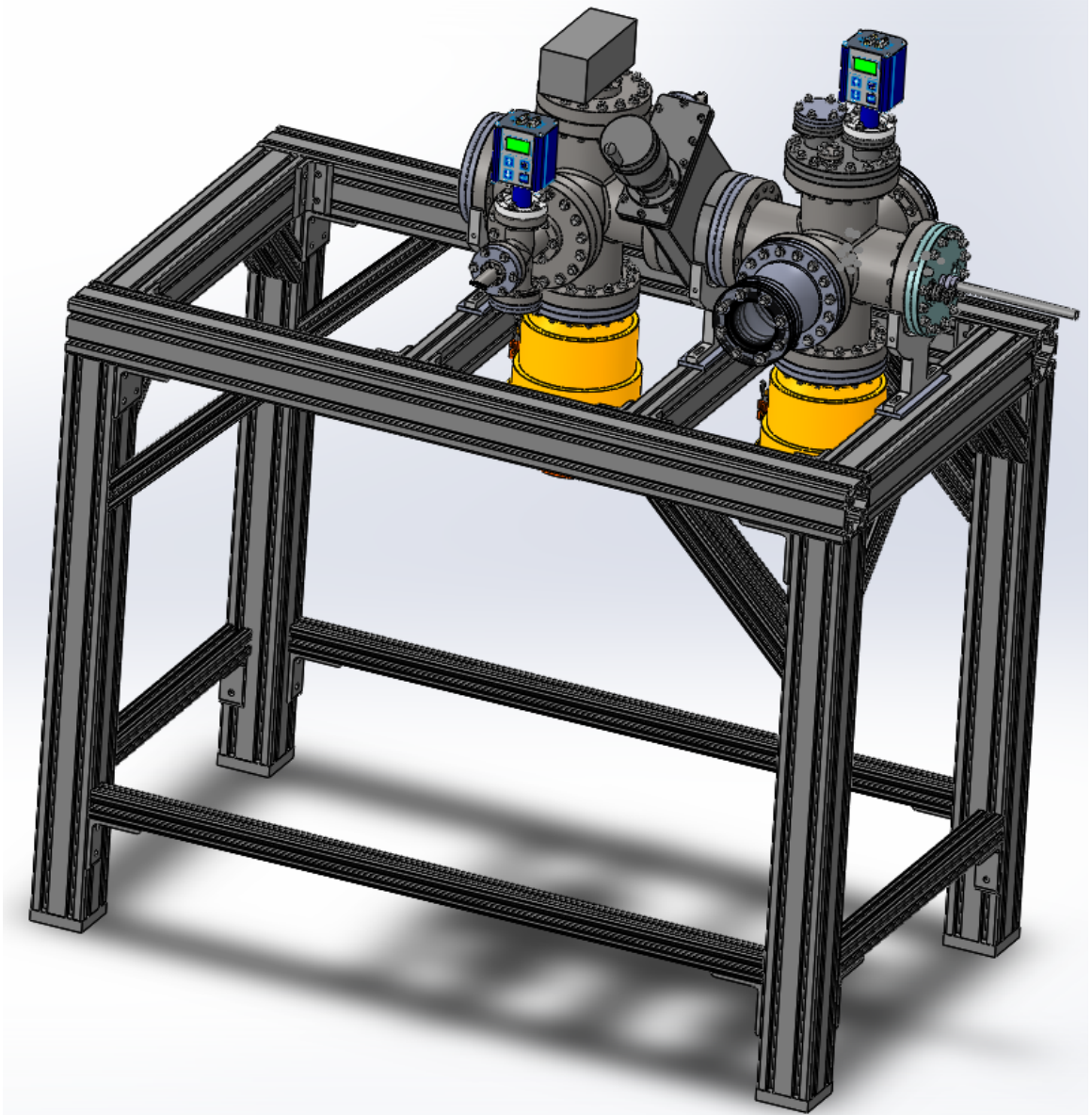


Figure 2.2: Apparatus supported by a custom built T-slot aluminum frame.

Assembly and machining

Many of the components that make up the assembly are built here at UNLV either in our lab or in the machine shop. Figures 2.3 & 2.4 are two examples of schematics that are made in the process of designing these components.

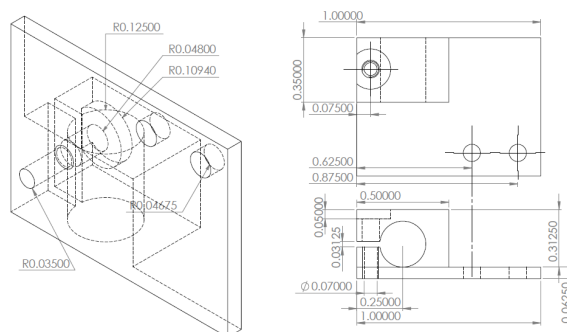


Figure 2.3: Schematic of clamp used to hold the picomotor.

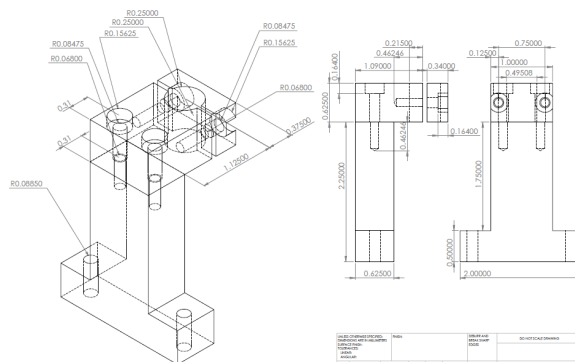


Figure 2.4: Schematic of clamp used to support and prevent rotation of the high pressure cell assembly.

Many components such as these are made by cutting an aluminum block with a CNC mill in the machine shop. Components that are central to the experiment, such

as the nozzle and high pressure cell, are machined from stainless steel for robustness.

Tantalum rod

One of the major considerations in the experimental design is the implementation of a source of Ta atoms. Laser ablation of a Ta rod is deemed suitable for this purpose. The Ta rod is attached to a picomotor which translates and rotates it to increase its lifetime. However, the physical properties of Ta makes it a difficult metal to machine. Drilling a hole into the Ta rod proves to be a challenge in of itself, thus our capability to work with this material is limited. Machining is limited to cutting an appropriate length of the rod, which is then glued to an aluminum adapter with a vacuum-compatible epoxy. A 3D-printed tube is used to keep the two pieces coaxial.

Picomotor control

The picomotor is responsible for translation and rotation of the rod to increase the amount of material that can be ablated by the laser. A fine-threaded screw is used for its smaller translation. Laser ablation of the Ta rod has been observed to whittle down the material very slowly, to the point that the picomotor could be operated at very minimal rates to sustain the ablation. Initially, the picomotor setup was intended to be fully automated, using sensors to determine the rod's range of motion. However, with the slow rates of the current setup, the need for automation was reduced, allowing for manual switching of the picomotor direction to suffice.

Supersonic jet nozzle

A supersonic molecular beam is the result of moving gas from a high pressure to low pressure region. As the gas transitions between the two regions, most of the random thermal motion of the gas molecules is converted into a unidirectional motion [12]. Consequently, the beam has a low internal temperature, as seen from an inertial frame along the beam.

The supersonic molecular beam is produced by introducing the prepared gas mixture into the high pressure cell shown in Figure 2.5. The high pressure cell is sealed from the rest of the vacuum chamber by two rubber o-rings, the inner one which translates to allow passage of gas into the chamber.

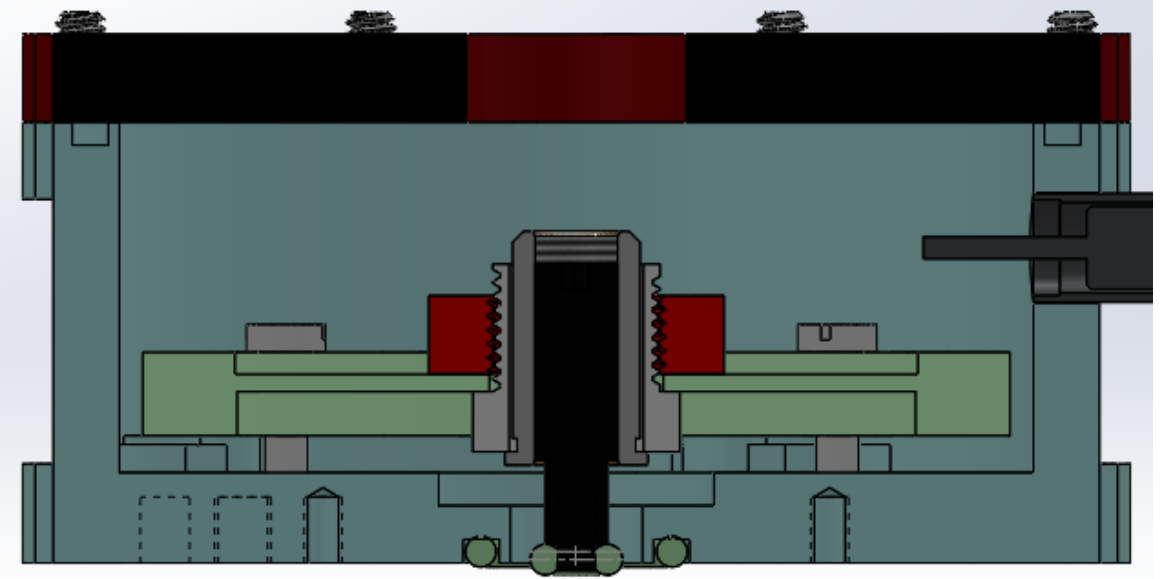


Figure 2.5: Cross-section view of the high pressure cell and PZT assembly. The gas mixture is introduced from above, and the source chamber is located below.

The PZT located inside the high pressure cell is responsible for providing short bursts of gas for the supersonic beam ($<100 \mu\text{s}$). The gas pulse duration is regulated to maintain the vacuum and allow the formation of the supersonic beam. Ideally, the duration of the gas pulse matches that of the ablation laser (5-10 ns) to maximize the production of TaO. The PZT valve is much better than its competitor solenoid in this regard ($>200 \mu\text{s}$). A longer diluted gas pulse may be used with the same effect of maintaining the vacuum, but is unfavorable in other aspects such as signal strength and cooling. A short concentrated pulse has a more pronounced signal in contrast to ambient noise.

Additionally, the supersonic beam is treated as an adiabatic, isentropic expansion at high source pressures. This gives the relationship

$$\frac{T_1}{T_0} = \left(\frac{\rho_1}{\rho_0}\right)^{\gamma-1} = \left(\frac{P_1}{P_0}\right)^{(\gamma-1)/\gamma} \quad (2.1)$$

where T is the temperature, P is the pressure, and ρ is the density of the gas [12]. The heat capacity ratio γ is 5/3 for monatomic gases such as He, Ne, and Ar. Assuming that the gas is at room temperature ($\sim 300 \text{ K}$), the peak pressure provided by the gas manifold is 100 PSI ($\sim 5000 \text{ torr}$), and the average vacuum during the duty cycle is on the order of 10^{-3} torr , the temperature of the supersonic beam can drop down to 1.6 K. If a long pulse 1/5 as dense as a short pulse at peak density was used, the temperature increases to 4.7 K. This demonstrates that a shorter pulse produces a lower supersonic beam temperature than a longer pulse with the same amount of

between pins 2&3, so the negative pulse can be transferred to an isolated part of the circuit with a floating ground. For the negative pulse to properly propagate to both of the optointerruptors, a 1K resistor is placed between the +12V supply and the optointerruptors to limit the current. The high and low values of the pulse produced by the optointerruptors are determined by the V_{CC} (8) and V_O (6) pins respectively, and for convenience the same positive voltage applied to V_{CC} is supplied to EN (7) to enable the input. For each optointerruptor, the positive voltages are defined by a preceding DC/DC converter (TMV2-1212SHI), which reproduces the voltage difference from the left side to the right. Both the optointerruptor and DC/DC converter electrically isolate the left and right sides, creating an isolated circuit for each of the optointerruptors. The transistors (IXBH10N170) are responsible for controlling the output voltage, such that the output is the high negative voltage for the duration of the pulse and ground otherwise. The preceding MOSFET drivers are responsible for supplying enough current to the transistors, and the bottom one is inverted to apply the correct logic such that the high negative voltage is the one being applied for the short duration of the pulse. When the PZT is supplied a negative voltage, the o-ring seal that is normally closed is opened, allowing the pressurized gas within the high-pressure cell to escape into the chamber.

One disadvantage is that the PZT is prone to deformation with the large pressure gradient it is exposed to. This will change the displacement dynamically in response to the vacuum of the chamber. The fine threads along the piston allows for in situ manual adjustment of its position to address this issue under vacuum.

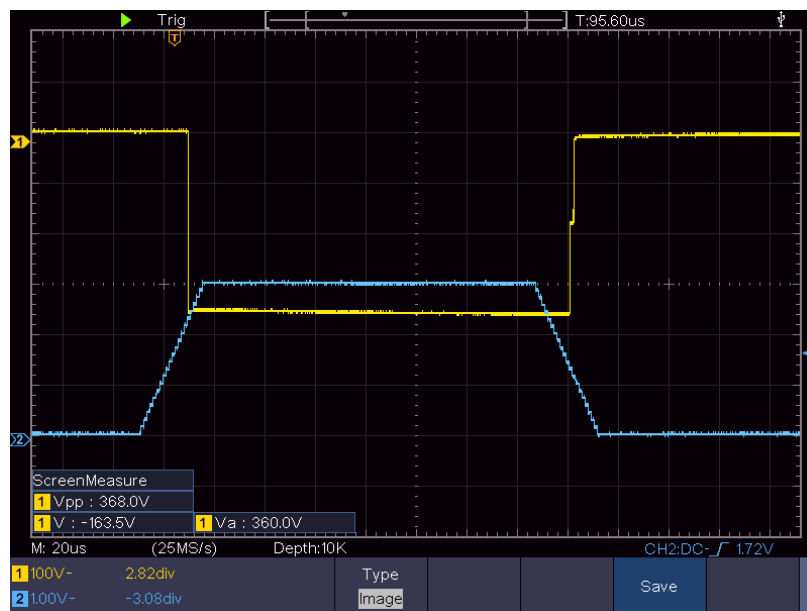


Figure 2.7: Voltage change without PZT.

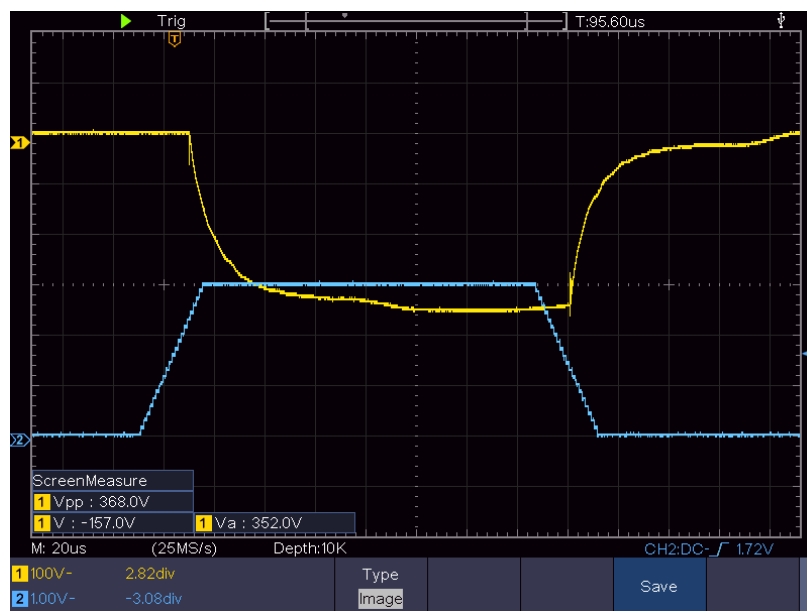


Figure 2.8: Voltage change with PZT.

At any instance, the PZT acts as the capacitor in an RC circuit, and thus the time it takes for the PZT to charge to 63% of the voltage is $\tau = RC$. Figures 2.7 and 2.8 show the potential (yellow) change in response to an external pulse (blue) with and without the PZT. The drop in potential indicates when the negative HV is supplied, and initially the potential is at ground. Without the PZT, the drop is near instantaneous, but with the PZT, there is a significant shark-finning that lasts around $50 \mu s$. With a resistance of 180Ω , $\tau \approx 10 \mu s$ and the capacitance of the PZT is estimated to be 55.6 nF . The manufacturer provided capacitance of the PZT (P-286.23) is $35 \text{ nF} \pm 20\%$. Reducing R can reduce τ but can lead to the issue of overshooting, where the voltage jumps past its original value before eventually returning to that value. The next smallest available HV resistor of 30Ω in the lab led to this issue. To improve this issue, a new valve with much smaller PZT that has sub-nF capacitance is under working for $10 \mu s$ pulse with $>300 \text{ PSI}$ backing pressure.

Ta rod ablation

The gas mixture leaving the high pressure cell enters the nozzle shown in Figure 2.9, which is also where TaO is produced. The Ta rod is attached to the picomotor, which is mounted on the high pressure cell as shown in Figure 2.11.

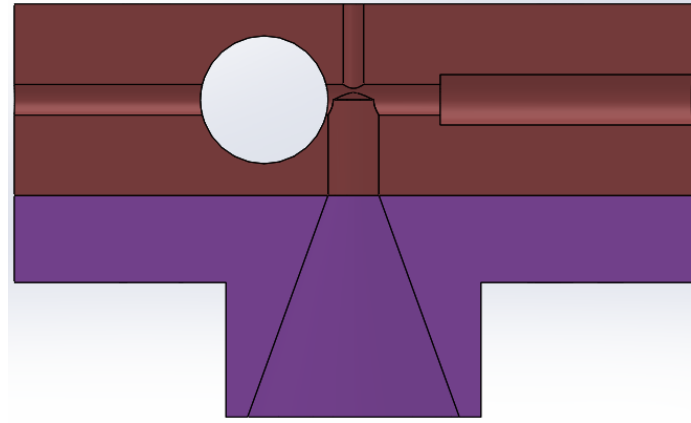


Figure 2.9: Cross section view of supersonic jet nozzle.

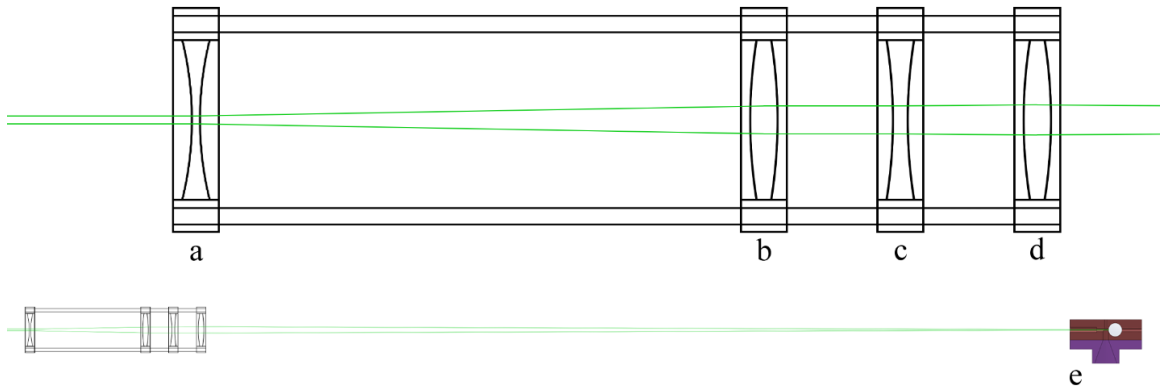


Figure 2.10: Optical setup for adjusting focal point of ablation laser. Focal point of lenses: a=-25 mm, b=125 mm, c=-100 mm, d=100 mm. e shows the focal point of the ablation laser in perspective with the supersonic jet nozzle.

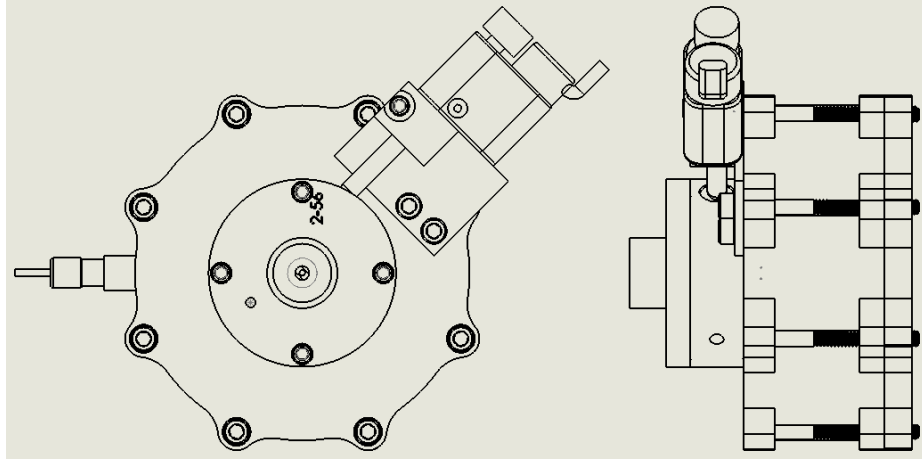


Figure 2.11: Schematic of high pressure cell assembly. (Move this figure to the laser ablation part)

The ablation laser is a pulsed laser with a fundamental of 1064 nm, which is then frequency doubled to obtain the second harmonic of 532 nm. The latter is more commonly used for many reasons; one being that it is visible, which is especially important for safety. For ablation to occur, the laser needs to be focused enough near the point of interest, but needs to pass through a glass window into the source chamber without damaging it. An optical setup shown in Figure 2.10 is used to achieve the aforementioned outcome. The initial concave lens diverges the laser and the subsequent concave lens collimates the laser to a diameter of 5 mm. This allows for finer adjustments to the focal position of the laser and greatly reduces damage to the window and optics. The third and fourth lenses are responsible for focusing the laser at the ablation site.

Two mirrors are used to align the laser. Operating the ablation laser at low power allows for alignment with the nozzle, which when successfully aligned shines through

the nozzle without the Ta rod. The ablation process involves precise synchronization of the gas pulse with the laser, which is explained in detail in the vacuum system and experimental results sections.

Photon collecting optics

The proximity and area of the photodetector means that only a very small fraction of photons reach it. To increase the efficiency of detecting photons, a parabolic mirror setup is used to redirect photons to the detector.

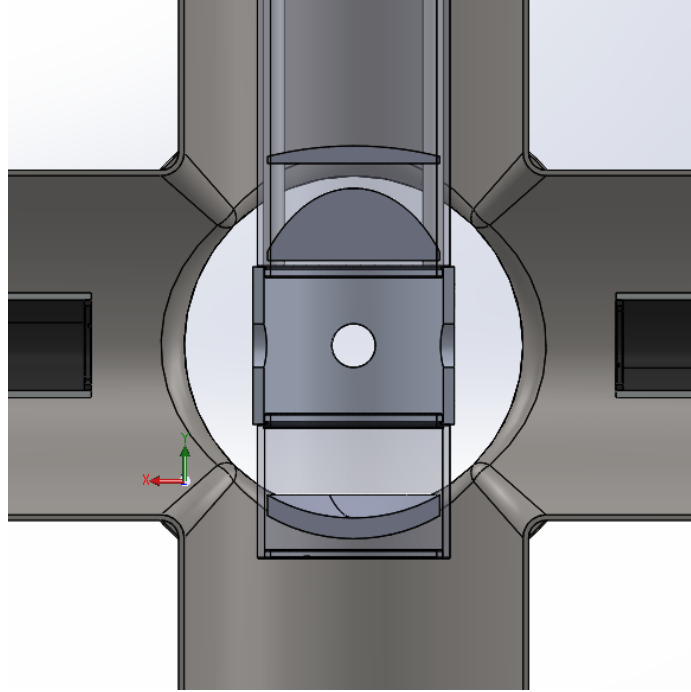


Figure 2.12: Cross section of parabolic mirror assembly situated in LIF chamber.

The mirror setup in Figure 2.12 is designed to optimize the amount of photons that reach the photodetector situated above. Laser excitation takes place inside a detection

cube at the center of the assembly, which has two small holes that allow the passage of ionization lasers. The detection cube is connected to lens tubes above and below, which houses the lenses and parabolic mirror. Photons which fall within the solid angle $\Delta\Omega = A/r^2$ subtended by the circular area of the overhead lenses are guided to a photodetector that rests above the LIF chamber. A parabolic mirror located below with its focus at the center reflects inbound photons back to the center towards the lens setup. The lenses and mirror have a 50 mm diameter. The distance/focus of the mirror is 50 mm, which yields a solid angle of $\pi/4 \pm 0.04$ sr (steradians). The distance of the flat end of the lens to the center is 24.66 mm, which yields a solid angle of 1.59 sr. The experimental solid angle efficiency, which is the fraction of photons expected to reach the photodetector, is 18.9%. This is obtained by dividing the solid angle coverage of the mirror setup by the maximum solid angle of 4π .

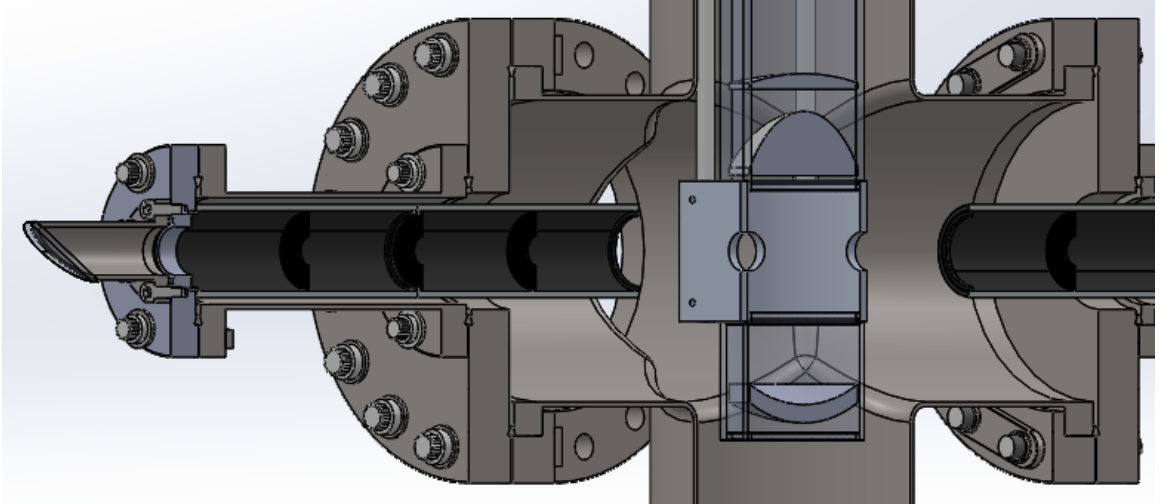


Figure 2.13: Cross section of parabolic mirror assembly situated in LIF chamber.

Shown in Figure 2.13 is a more complete view of the LIF chamber. One of the two Brewster windows are shown, which serves as an entryway for the excitation lasers. Light baffles are placed periodically along the laser path which reduces the amount of light scattered from the laser reaching the mirror setup, which can otherwise trigger the photodetector undesirably.

Gated PMT

Considering the small amount of photons that reach the photodetector, the signal is expected to be very weak. The photomultiplier tube (PMT) inside the photodetector amplifies this signal so that it may be seen in the oscilloscope. Structures in the PMT called dynodes are responsible for this amplification, producing additional electrons when hit by an incoming electron in a process called secondary emission. However, it is possible for the PMT to be triggered by other sources such as scattering from the lasers.

The PMT switch shown in Figure 2.14 effectively controls when the PMT should operate by controlling the potential of the first two dynodes D1&2. In a typical PMT, the dynodes form a potential gradient with a consistent difference between adjacent dynodes. In this particular PMT, the nine dynodes range from -900 to -100 V, with the photocathode at -1 kV and the anode near ground. This allows the electron generated by the photocathode to move to the anode through the potential gradient. The PMT switch can set the first two dynodes at a slightly higher potential of -1.02 kV to shut off this process. This capability allows the PMT to turn on only when a

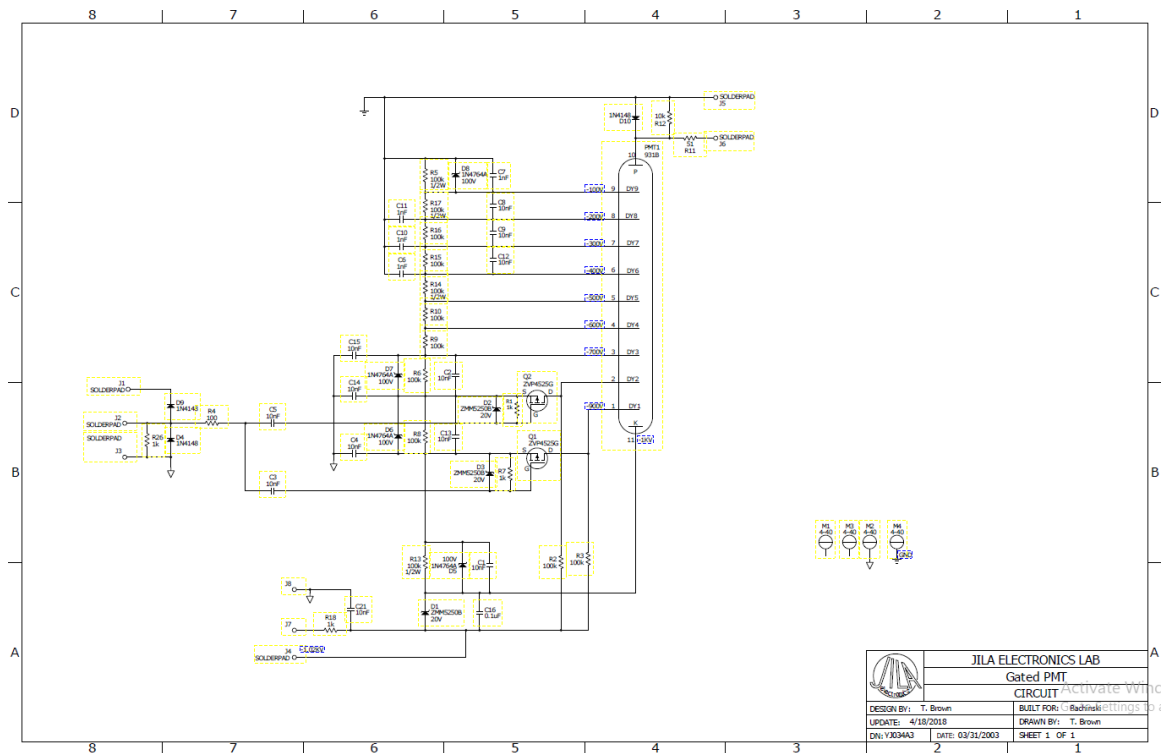


Figure 2.14: PMT switch circuit designed by JILA Electronics Lab.

TaO^+ signal is expected, which is triggered by a pulse in tandem with that generating the supersonic jet. This helps to reduce the likelihood of the PMT picking up stray photons.

Vacuum system

The vacuum system consists of a dry scroll vacuum pump which acts as a backing pump for two turbo pumps, one for each chamber. Turbo pumps have difficulties pumping down from atmospheric pressure, as their design makes them very sensitive to overheating.



Figure 2.15: Inner structure of a turbo pump. Reprinted from Wikimedia Commons.

As shown in Figure 2.15, the turbo pump consists of many bladed turbines, which rotate in alternating directions and kicks molecules downwards. The blades are designed to be as close as possible to the inner walls, to prevent any back-flow upwards into the vacuum chamber. However, this also makes the blades prone to scraping if they undergo thermal expansion, which limits the upper temperature limit of turbo

pumps to roughly 70 °C. In practice, it is best to avoid higher temperatures, and even 50 °C is avoided, so an interlock system is designed to shut down the vacuum system past certain thresholds to prevent damage to the turbo pumps. The backing pump helps to keep the turbo pumps from overheating by reducing the number of molecular collisions with the turbine blades.

Achieving a high vacuum is more involved than simply pumping down the chambers. Gaseous molecules can remain trapped in the microscopic structure of the inner walls, or be generated by contaminants. Both can compromise the vacuum for several days to weeks, necessitating a method to resolve these factors.

Baking system

Baking the vacuum chambers is a solution to free trapped gaseous molecules from the inner walls. This facilitates the initial pumping process, reducing the waiting period to between several hours and a few days.

While baking is primarily done on the 6-way junction tube that houses the components, there are still different temperature tolerances for different parts of the tube. Being able to bake while monitoring the temperature of each part is crucial to preventing damage to sensitive parts, necessitating the usage of thermocouples. A diagram of the baking/monitoring feedback is given in Figure 2.16, where an Arduino board monitors the temperature of various parts and switches on/off the heating tapes responsible for heating the chambers.

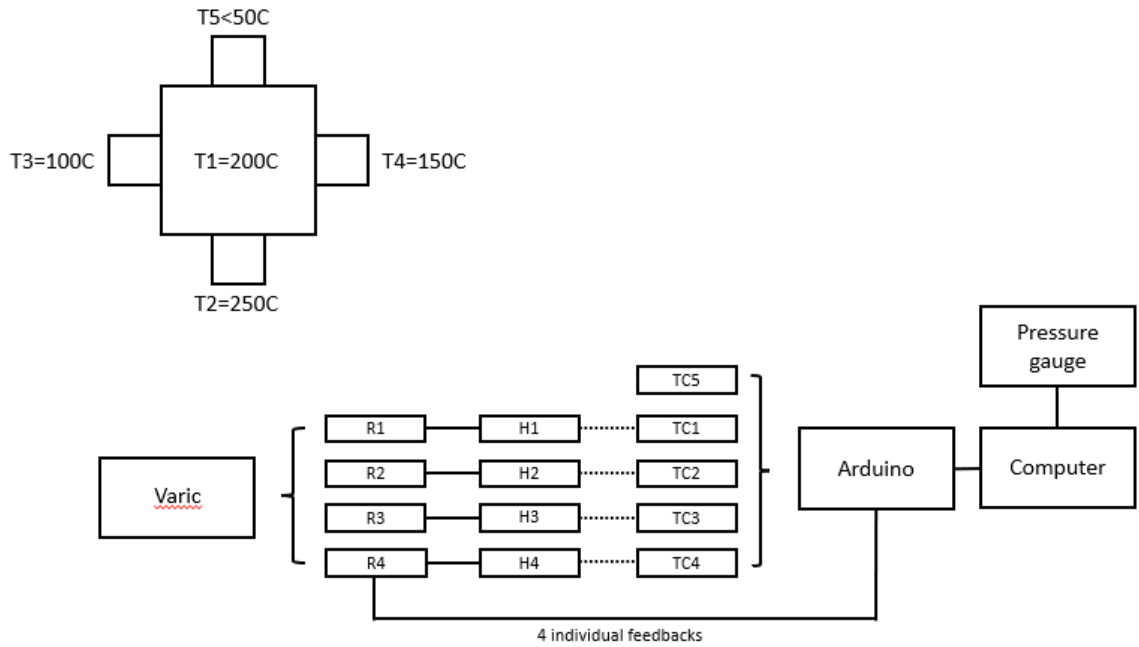


Figure 2.16: Diagram of baking system.

Spectroscopic laser system

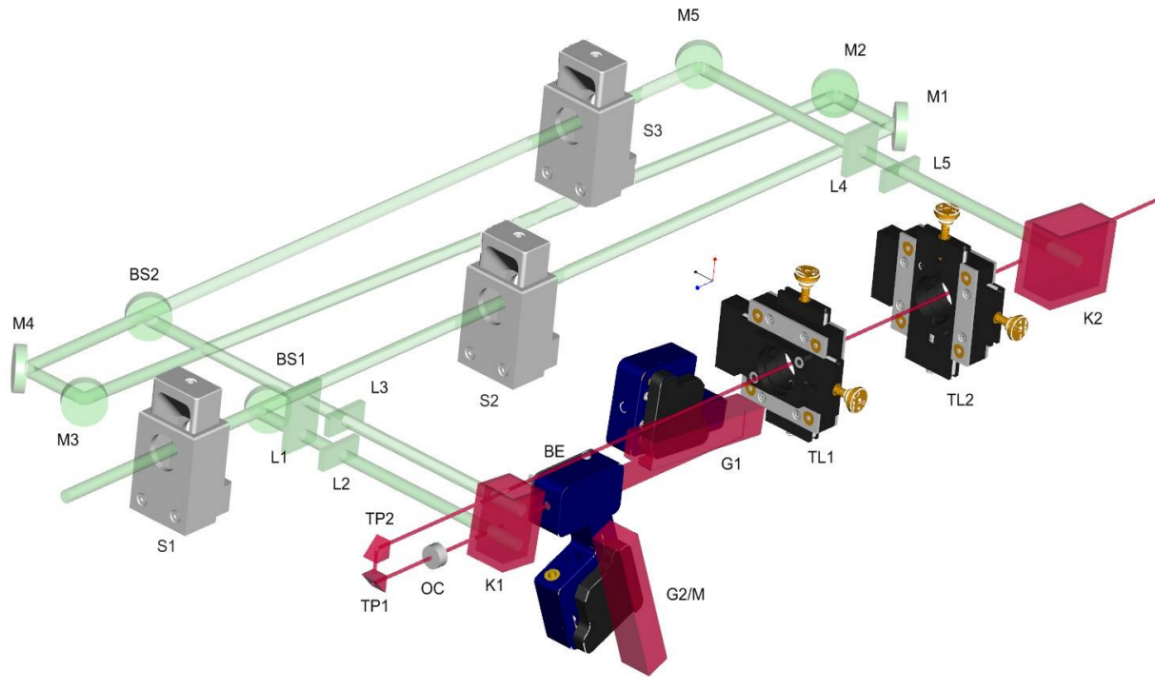
Nd:YAG laser

The Nd:YAG (Neodymium-doped Yttrium Aluminum Garnet) laser has a wavelength of 1064 nm. While there are competing transitions at other wavelengths such as 1319, 1338, and 946 nm, they have lower gain and a higher threshold [13]. The flashlamp and Q-switch are two essential components of the YAG laser. Frequency conversions, such as second harmonic generation (SHG), third harmonic generation (THG), and fourth harmonic generation (FHG), are used to produce 532, 355, and 266 nm wavelengths from the original 1064 nm wavelength. For example, to generate 532 nm light, the fundamental laser beam is sent through a nonlinear KD*P crystal with a precisely controlled phase match angle [13].

I use the model Spectra-Physics Lab-190, at a rep rate of 10 Hz, which produces an energy of 300 mJ/pulse at 532 nm. The flashlamps of the Nd:YAG laser is optimized to work at full power, producing consistent results when operating at such conditions. Otherwise, there are fluctuations that arise from temperature deviations in Nd:YAG rod and frequency conversion crystals. The typical output power of the Nd:YAG laser at 532 nm is 2 W, but as the Nd:YAG laser serves as a pump laser for the Liop-tec dye laser, the power is lowered to match the specifications of the latter. A half waveplate and a polarizing beam splitter are used to reduce the laser power prior to subsequent usages, and the excess laser is directed to a beam dump.

LIOPTEC dye laser

The LIOPTEC dye laser is readily tunable to cover a wide range of frequencies, unlike the Nd:YAG laser. However, it requires a pump laser to operate, namely the Nd:YAG laser. As its name suggests, the dye laser uses a dye which fluoresces from exposure to the pump laser to produce a laser of a different wavelength. As shown in Figure 2.17, the pump laser is fed into two dye cells, the first (K1) which creates the dye laser and the second (K2) which amplifies the output. The laser produced by K1 exhibits a spectrum of frequencies, which is tuned with a diffraction grating to output a specified frequency prior to entry into K2.



M1-M5: HR-Mirror

BS1-2: Beamsplitter

L1, L4: Expanding Lenses

L2, L3, L5: Focusing Lenses

G1: Grazing Incidence Grating

G2/M: Littrow Grating or Tuning Mirror

BE: Beam Expander

OC: Output Coupler

TP2/2: 90° Turning Prism

TL1, TL2: Telescope Lenses

K1: Oscillator and Preamplifier Dye Cell

K2/B: Main Amplifier Dye Cell

S1-S3: BeamShutter

Figure 2.17: Optical configuration of the dye laser [3].

Dyes

The various dyes used in the dye laser determine the range of wavelengths it may take on. An appropriate dye needs to be able to fluoresce from the pump laser wavelength, which then produces a spectrum. Rhodamine 101 is one such example, with a tuning range of 614-650 nm and a pump wavelength of 532 nm [3].

Grating (tunability, cavity, distinguish from other dye lasers)

The Nd:YAG laser coming from the bottom focusing lens (L2) is responsible for initializing the dye laser. A cavity is formed with an output coupler (OC) at one end and a tuning mirror (M) at the other. The dye laser is sent along a 1800 line/mm grazing incidence grating (G1) in the Littman configuration [14], positioned such that the beam spans the length of the grating. The grating structure illustrated in Figure 2.18 causes the laser to diffract at multiple angles, where constructive interference peaks.

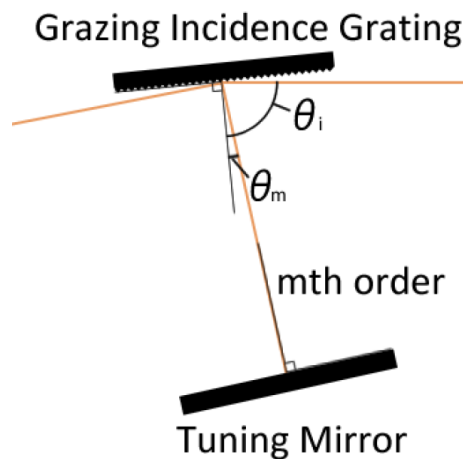


Figure 2.18: Diagram showing the mth order diffraction of the grating.

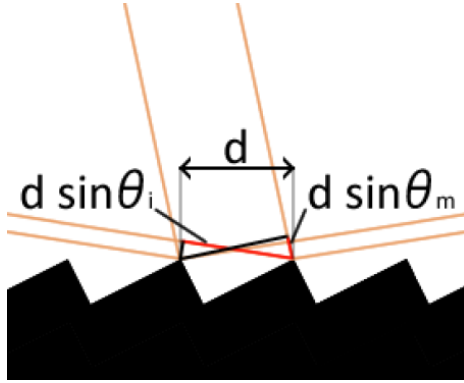


Figure 2.19: Diagram showing the path difference between adjacent reflected beams.

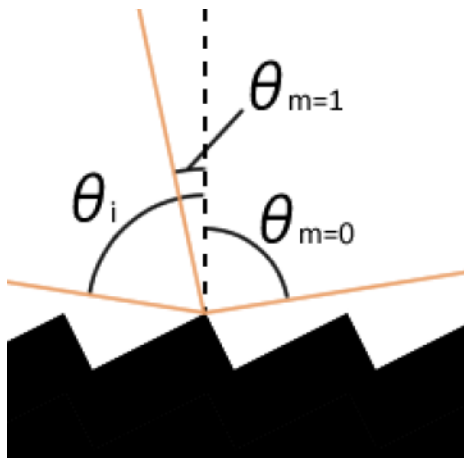


Figure 2.20: Diagram showing the diffraction orders of a 624 nm laser.

Figure 2.19 shows the path difference between two adjacent diffracted beams. The condition for constructive interference can then be determined as:

$$d(\sin \theta_i - \sin \theta_m) = m\lambda \quad (2.2)$$

where d is the distance between two adjacent lines, m is an integer that represents the order of diffraction, λ is the wavelength of the laser, θ_i is the angle of incidence, and θ_m is the angle corresponding to the m th order of diffraction. The negative sign comes from the coordinate choice of the reflected angle being positive clockwise to the normal of the grating. This equation is also known as the grating equation, and can be rearranged to solve for the angle of the m th diffraction order:

$$\theta_m = \arcsin \left(\sin \theta_i - \frac{m\lambda}{d} \right) \quad (2.3)$$

Given the range of wavelengths produced by the Rhodamine 101 dye, the only possible modes of diffraction are the 0th and 1st order. The zero-order mode is independent of wavelength, where the laser treats the grating like a mirror. The 1st order is of primary interest, which yields angles roughly from -6° to -10° . These orders of diffraction are shown in Figure 2.20.

The tuning mirror is responsible for reflecting the diffracted beam back along the beam path. As the different wavelengths of the diffracted beam correspond to different values of θ_m , the tuning mirror is able to selectively reflect back a specific wavelength. The angle of the tuning mirror can also be adjusted to change which wavelength is reflected back, allowing the dye laser to change frequencies within the fluorescence spectrum of the dye.

Non-linear optical crystal, frequency doubling, UV light

Like the YAG laser, the LIOPTEC dye laser uses a nonlinear crystal to produce frequencies in the UV range as shown in Figure 2.21.

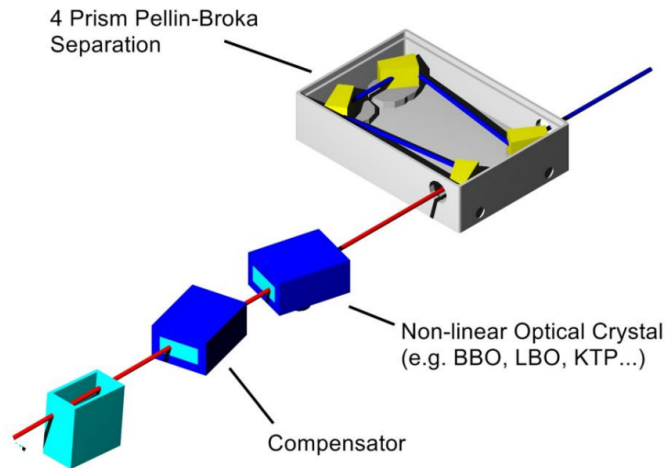


Figure 2.21: Non-linear optical crystal for frequency doubling and a compensator to correct the beam path [3].

The UV laser propagates parallel to the dye laser fundamental, necessitating the separation of the beams. This is done through a four prism Pellin-Broka separation which isolates the UV laser using the difference in refraction angles.

ASE

To obtain a very good beam profile, optimizations are made to the oscillator dye cell (K1). Amplified spontaneous emission (ASE) is fluorescence of the dye that is amplified in the oscillator. This is often undesirable, such as in our case, and one optimization of the laser involves reducing the ASE relative to the actual laser as

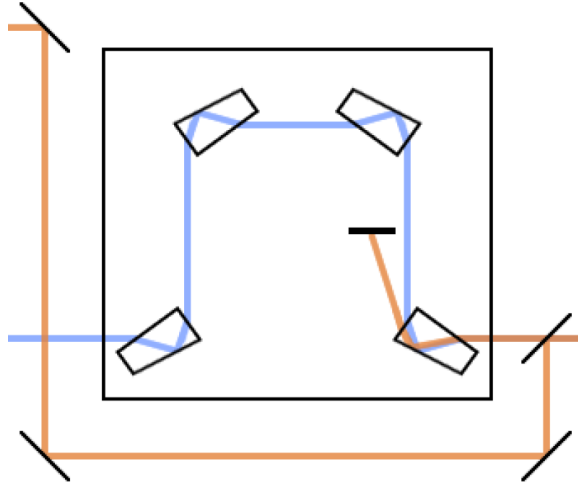


Figure 2.22: Trajectory of dye laser and its second harmonic in a Pellin-Broka prism arrangement.

much as possible. This is done by propagating the laser at an angle to the direction of the ASE such as shown in Figure 2.23. However, a greater angle will reduce the energy conversion of the oscillator, so a balance must be achieved between this and the ASE background.

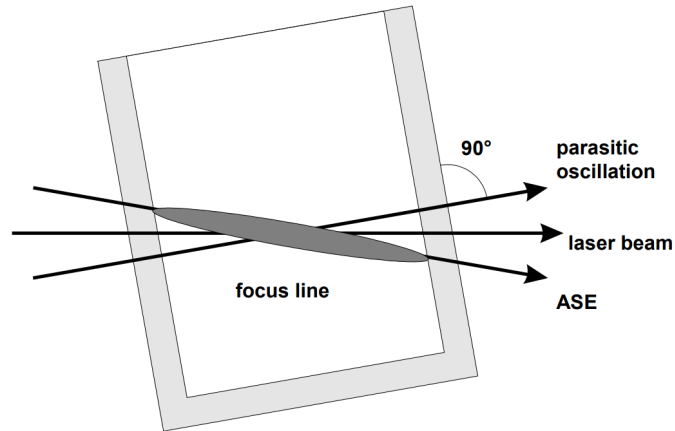


Figure 2.23: Diagram showing the orientation of the ASE and laser beam. The grey region is the area exposed to the Nd:YAG laser, which is passed through a cylindrical lens. The parasitic oscillation arises between the dye cell walls [3].

Dye laser wavelength characterization

Motivations

- Lioptec pulsed dye laser FSR.
- Using a 1800 line/mm or 2400 line/mm grating, the optimized laser linewidth is about 0.06 cm^{-1}
- How many modes exist for the multi-mode laser?
- The number of the excited modes is not only determined by the grating groove number, but also determined by the beam alignment in the cavity.
- A device that can monitor the linewidth, or the number of the excited modes, is critical for optimizing the dye laser alignment.
- This laser will be tuned from 450 nm to 900 nm. A well-characterized device is required to measure the laser wavelength in this broad regime.

To meet the above mentioned requirements, I will first discuss a home-built linewidth measurement device called the monitor Etalon which probes and optimizes the laser linewidth. Then I will compare the relative central wavelength changes measured by a commercial wavelength meter and the monitor Etalon. Last, I will show that our wavelength measurement system can reliably obtain the dye laser wavelength better than 10 cm^{-1} , which will allow for resolving individual rotational states.

Monitor etalon

The optical cavity is a sensitive device to discriminate optical frequencies using interference. There are two well-applied configurations for this purpose, scanning Fabry–Pérot cavity and monitor Etalon. The former one is scanning cavity resonant frequency to extract all possible laser frequencies sequentially by observing cavity transmission on an oscilloscope in the time-domain. The Fabry–Pérot cavity is typically used for continuous wave lasers and its frequency resolution is always high (Finesse is 100 or more) [15]. The latter one is a fixed Fabry–Pérot cavity that consists of two parallel partially reflecting surfaces with a fixed distance. The frequency discrimination comes from the spatial interference from a tilted incident light beam, as shown in Figure 2.24. The spatial interference can be recorded by a camera as a pattern of concentric rings, as shown in Figure 2.24. Typically, the monitor Etalon is used for pulsed laser and its frequency resolution is relatively low (Finesse is 30 or less).

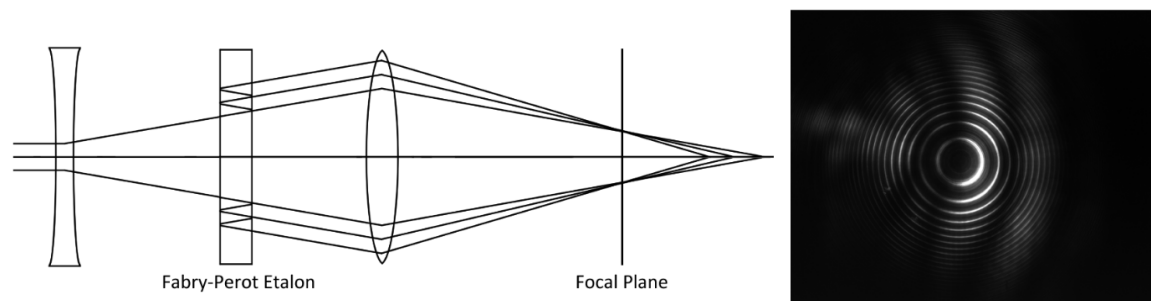


Figure 2.24: Path of laser going through the monitor etalon. Constructive interference may occur at multiple angles bounded by the path of the laser.

Figure 2.24 shows a diagram of our home-built monitor Etalon. The input laser beam is firstly diverged by a concave lens ($f=-25$ mm). The monitor Etalon creates a large number of mutually coherent beams by division of amplitude. This is due to the semitransparency of the two mirrors, which allow for partial transmission and reflection. These beams are then converged using a convex lens ($f=50$ mm), which creates interference where they overlap. At specific angles produced by the convex lens, constructive interference occurs, each angle converging at different distances away from the optical axis. This creates a set of concentric rings called interference fringes, shown in the right of Figure 2.24. As will be explained later on, the distance where mutually coherent beams converge remains constant for any angle created by the concave lens. This is shown as the focal plane, where a camera can record the image of the interference fringes. The camera is triggered with a pulse generator which is then optimized to collect each pulse of the laser with minimum exposure to ambient light. This circumvents certain issues such as displaying multiple pulses on the same image, which can saturate the image and cause potential issues such as misrepresenting the width of the interference fringes.

An ABCD matrix is used to calculate the trajectories of angled parallel rays on a convex lens using

$$\begin{pmatrix} 1 & d \\ 0 & 1 \end{pmatrix} \cdot \begin{pmatrix} 1 & 0 \\ -1/f & 1 \end{pmatrix} \cdot \begin{pmatrix} a \\ \theta \end{pmatrix} \quad (2.4)$$

where d is the distance between a plane and the thin lens, f is the lens, and a and θ are the y-position and angle of the ray at the lens [15]. Evaluating this matrix gives

$$\begin{pmatrix} a(1 - \frac{d}{f}) + d\theta \\ -\frac{a}{f} + \theta \end{pmatrix} \quad (2.5)$$

The matrix is evaluated for multiple values of a to obtain the trajectories of multiple parallel beams, and any two matrices can be compared to find the position where they intersect. For two arbitrary values a and b , the condition for intersection is defined as

$$(a - b)(1 - \frac{d}{f}) = 0 \quad (2.6)$$

which leads to $d=f$ as the solution. This shows that all rays converge at the focus of the convex lens, at a height of $d\theta$. As the ABCD matrix is derived using the paraxial approximation, these results are valid only at small angles where $\sin \theta \approx \theta$. This is the case for this situation, where the incident angles of the interference fringes are on the order of milliradians.

The height at which constructive interference occurs can be obtained from the above equation, taking into account the beam trajectory preceding the convex lens. This can be taken for each of the interference fringes, and compared to those in the images obtained from the camera. Doing so validates the consistency between

the model and apparatus, and provides the interference pattern expected for a given laser frequency. This frequency is then compared to the reading of the wavemeter as another method to check its reliability.

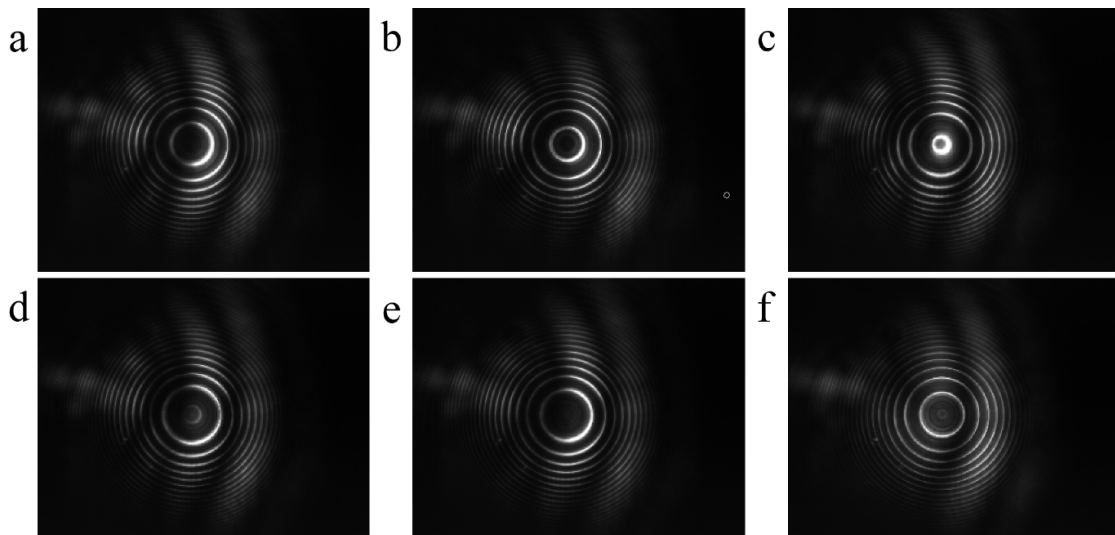


Figure 2.25: Interference fringes for 624.5588 nm (a), 624.5625 nm (b), 624.5662 nm (c), 624.5700 nm (d), 624.5740 nm (e), and 624.5779 nm (f). Spacing between fringes is nonlinear but corresponds to the same resonance frequency.

Figure 2.25 shows multiple images of interference fringes collected by the camera. By adjusting the wavelength of the dye laser, images can be collected over a range of frequencies, from which shifts in the fringe positions can be observed. These interference fringes can then be used to determine the linewidth of the laser, as well as measure frequency shifts.

The linewidth corresponds to the width of the peaks, and the frequency shift corresponds to the shift in peak positions when changing the laser frequency.

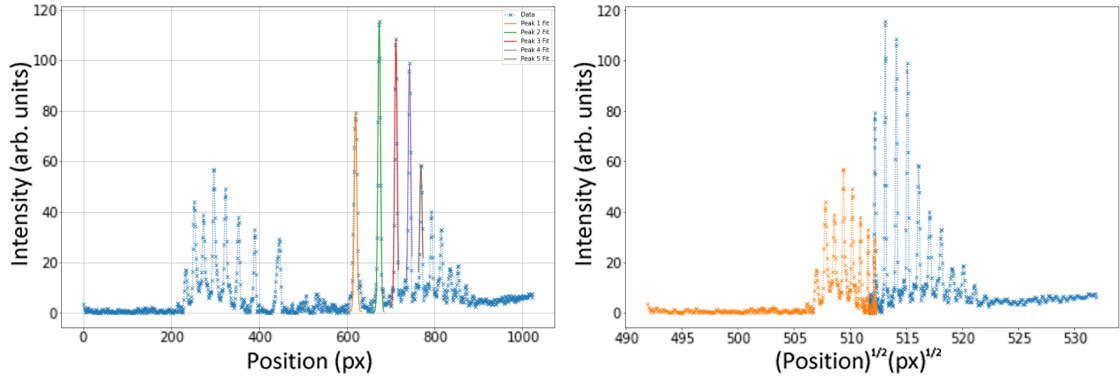


Figure 2.26: Left: Vertical slice across the center of interference fringes. Position is in pixels and intensity is the sum of RGB values. Right: x scale has a correction to the non-linearity so that peaks are equidistant.

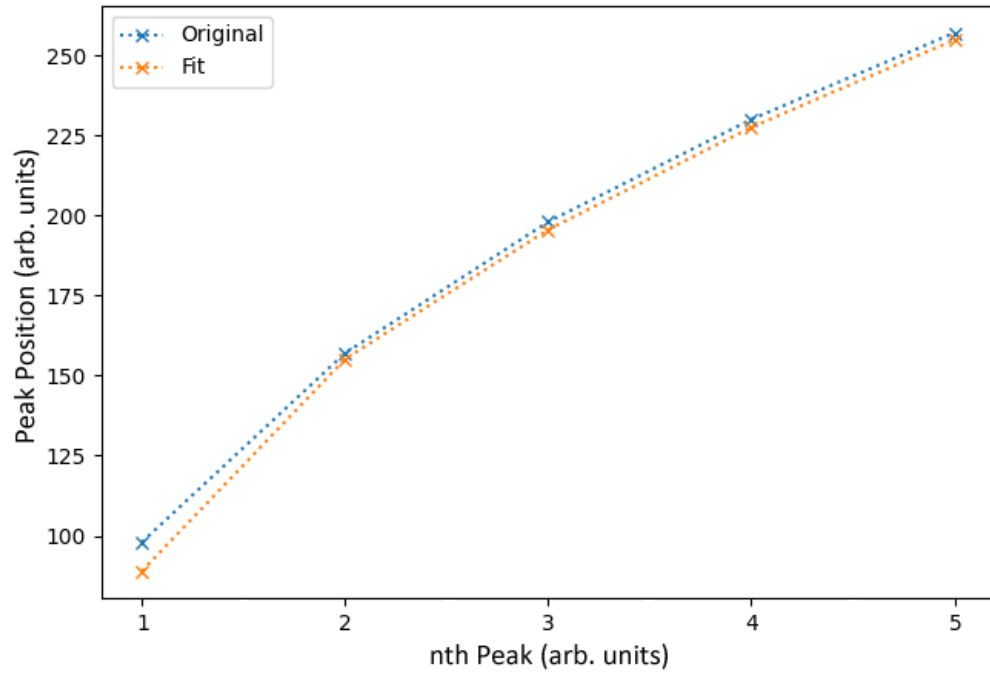


Figure 2.27: Comparison of peak position vs peak enumeration for the original data and a function obtained from curve fitting. Peak position is taken as the distance in pixels from the center of the interference fringes.

The non-linearity can be corrected by fitting the peak positions to a test function. First, data is taken from a vertical slice of the interference fringes and plotted as intensity versus position, shown on the left of Figure 2.26. A set of peaks either left or right from the center are used to find the test function by plotting the peak positions with respect to the center versus an appropriate enumeration depending on the trial function, given as the blue curve in Figure 2.27. A trial function of the form

$$y = a\sqrt{x - b} + c \quad (2.7)$$

is used where a, b, and c are fitting parameters for the curve fit. This is then plotted for comparison as the orange curve in Figure 2.27. The inverse function of (2.7) is then applied separately to the left and right halves of the x-axis in the original plot, shown in the left of Figure 2.26, to obtain the corrected plot on the right. As an additional check, the peak distances are taken for each set of adjacent peaks, and the mean and standard deviation are taken. Generally a coefficient of variation of 0.05 is deemed acceptable. The average can then be used to obtain a frequency shift that is much more consistent with the wavemeter than the non-linear measurements.

The linewidth of the laser is given by $0.5/w*d$, where the w is the average peak width and d is the distance between a pair of neighboring peaks. This linewidth is expected to be consistent for any applicable pair, and so an average linewidth can be obtained over multiple peaks. The peak width may be obtained by the FWHM, but a better method involves using Gaussian fits, where the width can be derived from

its parameters.

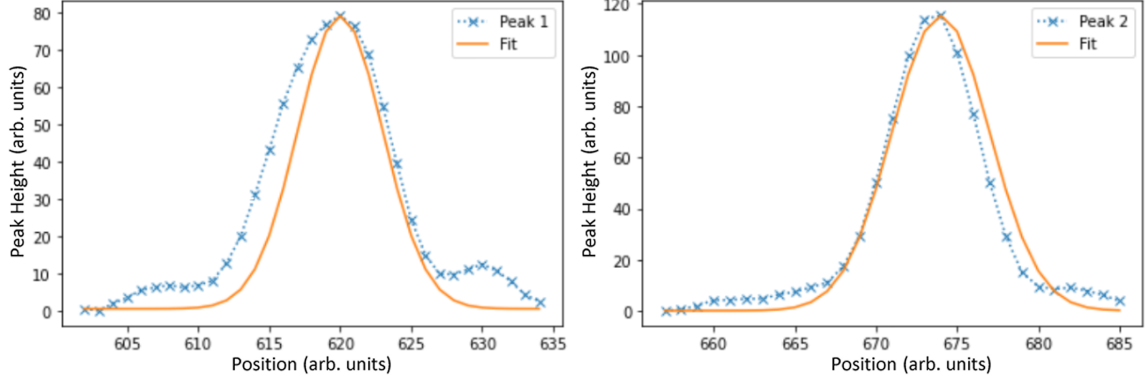


Figure 2.28: Closer view of the first two peaks to the right of the center. Peak widths are obtained through Gaussian fits.

From measuring the displacement of these fringes with respect to the change in laser wavelength, a visually determined frequency shift can be obtained with the expression:

$$\Delta f_e = \frac{x_{p1\lambda 2} - x_{p1\lambda 1}}{x_{p2\lambda 1} - x_{p1\lambda 1}} * 15[\text{GHz}]$$

where x is the position, $p1$ and $p2$ are the first and second peaks, and $\lambda 1$ and $\lambda 2$ are the wavelengths of two adjacent images. 15 GHz is the resonance frequency of the etalon, determined by the manufacturer.

The minimum observed laser linewidth is 0.068 cm^{-1} , or 2.04 GHz, which is much lower than the difference between adjacent rotational states. The wavelength scanning settings of the dye laser will not always be consistent to the actual wavelength shifts,

and so a wavelength meter is used to monitor the wavelength. The interference fringes have confirmed that the wavelength shifts measured by the wavelength meter are consistent with the actual shifts.

Comparison between monitor Etalon and High-Finesse WS7-60 wavelength meter

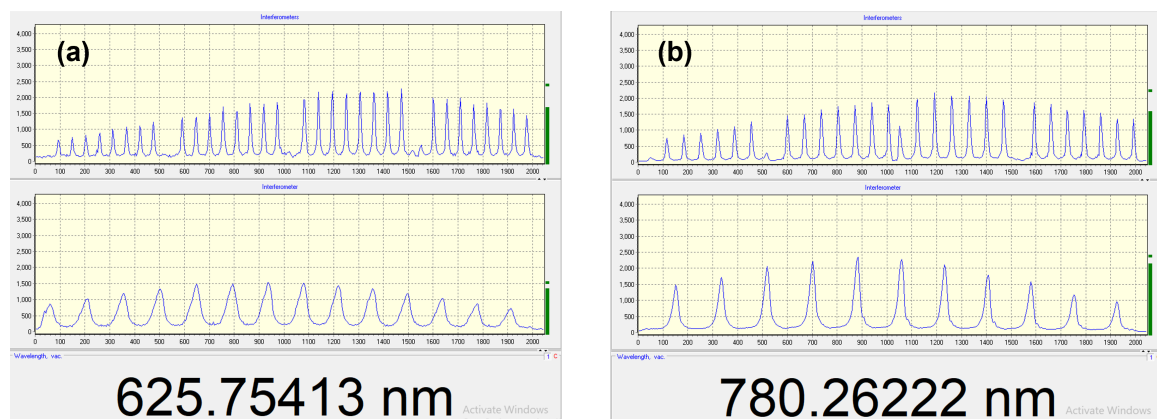


Figure 2.29: Wavemeter comparison between a) dye laser and b) a single mode 780 nm laser. Upper and lower plots correspond to low and high-resolution Fizeau wedges respectively [4]. Horizontal axis represents the position of the interference signal (arb. units) and vertical axis is the relative intensity of the signal (arb. units).

This shows that the WS7-60 wavemeter, which is typically used for single mode cw lasers, can be used to measure the pulsed dye laser. However, using the wavemeter in this way warrants caution as the wavemeter only accepts a single mode fiber, which can still be used without being damaged as long as the dye laser is carefully attenuated. The averaging time of the wavemeter is also relatively long (1s), which should be considered when scanning across frequency ranges during data acquisition.

Wavelength (nm)	Etalon shift (GHz)	Wavemeter shift (GHz)
624.5779	2.7	3.0
624.5740	3.0	3.1
624.5700	3.1	2.9
624.5662	2.5	2.8
624.5625	2.9	2.8
	Average (GHz)	σ (GHz)
Etalon	2.8	0.2
Wavemeter	2.9	0.1

Table 2.1: Comparison of frequency shifts from the monitor etalon and wavemeter measurements.

Absolute wavelength measurements

The WS7-60 wavemeter is calibrated weekly with the Rb D1 transition. The absolute wavelength accuracy is 60 MHz, which is much better than the linewidth of the dye laser.

Interference fringes and etalon

The linewidth of a laser characterizes its range of frequencies. A smaller linewidth allows for more precise excitation of atoms to a single desired state, while a larger linewidth may encompass multiple excitations which can affect the population of excited states. A smaller linewidth is not always better: Some applications benefit from having a larger linewidth.

Timing system

The timing and duration of the pulses discussed so far is determined a BNC Model 577, Digital Delay and Pulse Generator which has 8 synchronizable channels. Two channels are dedicated to the Q-switch and flashlamp trigger of the YAG laser. Another two are responsible for those of the ablation laser. Other channels control the timing for the supersonic beam nozzle, PMT switch, and oscilloscope. Parameters for Ta are given for these channels as:

ChE, ablation flashlamp: $T_0 + 10 \text{ ms}$

ChF, ablation Q-switch: $\text{ChE} + 110 \text{ } \mu\text{s}$

ChG, nozzle: $\text{ChF} - 490 \text{ us}$, pulse width= $250 \text{ } \mu\text{s}$

ChB, Nd:YAG Q-switch, $\text{ChF} + 690 \text{ } \mu\text{s}$

ChA, Nd:YAG flashlamp, $\text{ChB} - 130 \text{ } \mu\text{s}$

ChH, PMT switch, $\text{ChB} - 0.75 \text{ } \mu\text{s}$, pulse width= $1 \text{ } \mu\text{s}$ (falling edge trigger)

ChC, Scope trigger, $\text{ChB} + 0 \text{ } \mu\text{s}$

while those of TaO with 0.8% O₂ in Ne gas mixture has the following modifications:

ChG, nozzle: $\text{ChF} - 357 \text{ } \mu\text{s}$, pulse width= $270 \text{ } \mu\text{s}$

ChB, Nd:YAG Q-switch, $\text{ChF} + 430 \text{ } \mu\text{s}$

The timing of these pulses are also shown in Figure 2.30 for TaO.

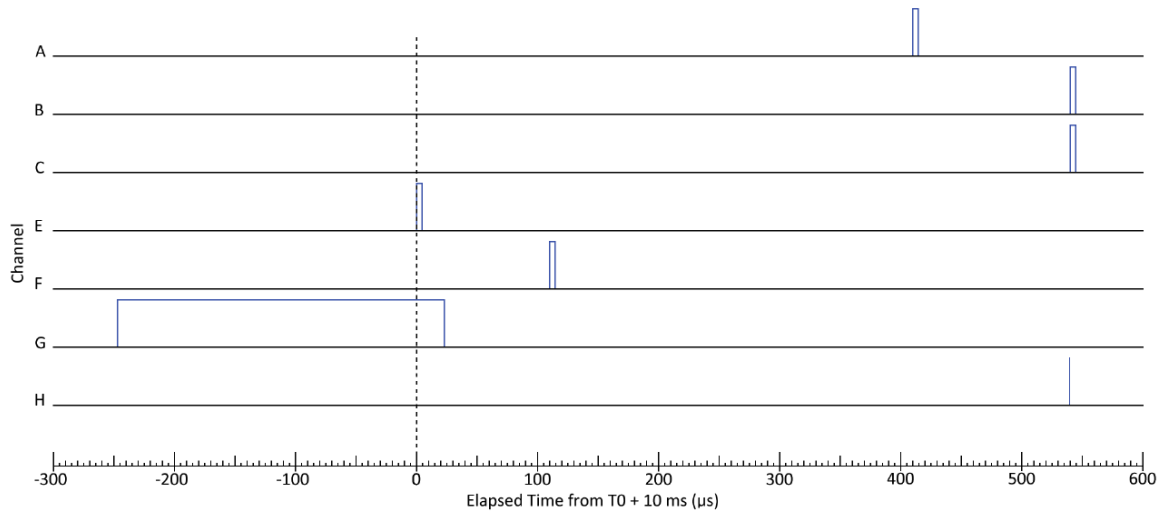


Figure 2.30: Timing of pulses in pulse generator for TaO.

In particular, ChG is responsible for synchronizing the Ta rod ablation with the gas pulse and ChB controls the timing of the ionization laser pulse with respect to that of the ablation laser. The latter is expected to change because of the different masses of Ta and TaO, and the former is especially important for the formation of TaO. These parameters are optimized experimentally, as explained in the next section.

CHAPTER 3

EXPERIMENTAL RESULTS

Optimizations

As the signal is expected to arrive in pulses, there will be an optimal delay between the creation of the gas pulse and activation of the PMT gate. As the maximum pressure from the gas manifold is controlled, the supersonic beam speed is expected to remain constant as long as there is a sufficient supply of the gas mixture. Initially, the process involves looking for a known Ta signal based off the NIST chemistry database, where I use Ta instead of TaO for the former's abundance over the latter. Scanning through the delay times should result in a peak signal strength at a certain point, which can then be used for subsequent experiments.

Ta and TaO

The purpose of this experiment is to serve as a precursor for subsequent projects on high-resolution laser spectroscopy. A scan over the frequency range of the dye in the dye laser yields a signal from the photodetector which corresponds to photons emitted from excitation. For each frequency, 20 photodetector readings from the oscilloscope are summed then integrated using the composite trapezoidal rule. This serves as a method to count the number of photons detected, as the signals produced are identical to each other.

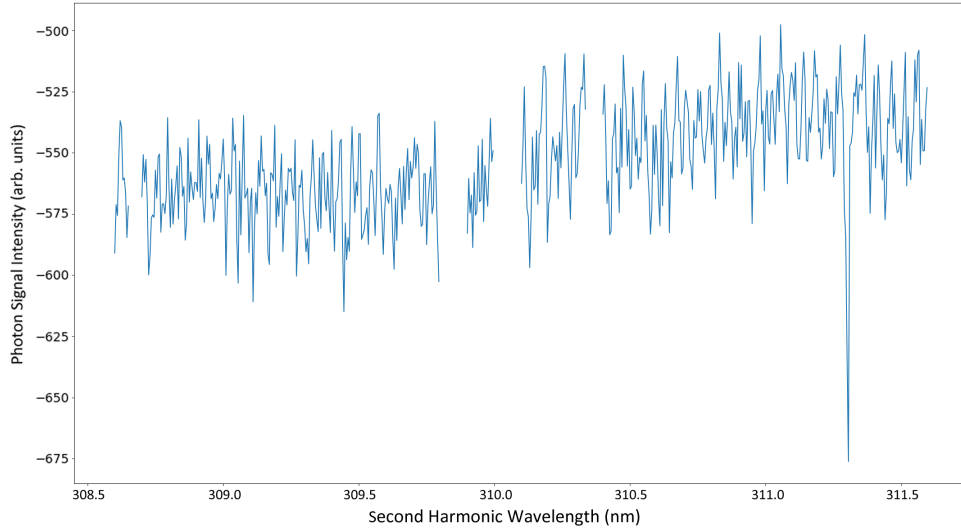


Figure 3.1: Photodetector readings without oxygen.

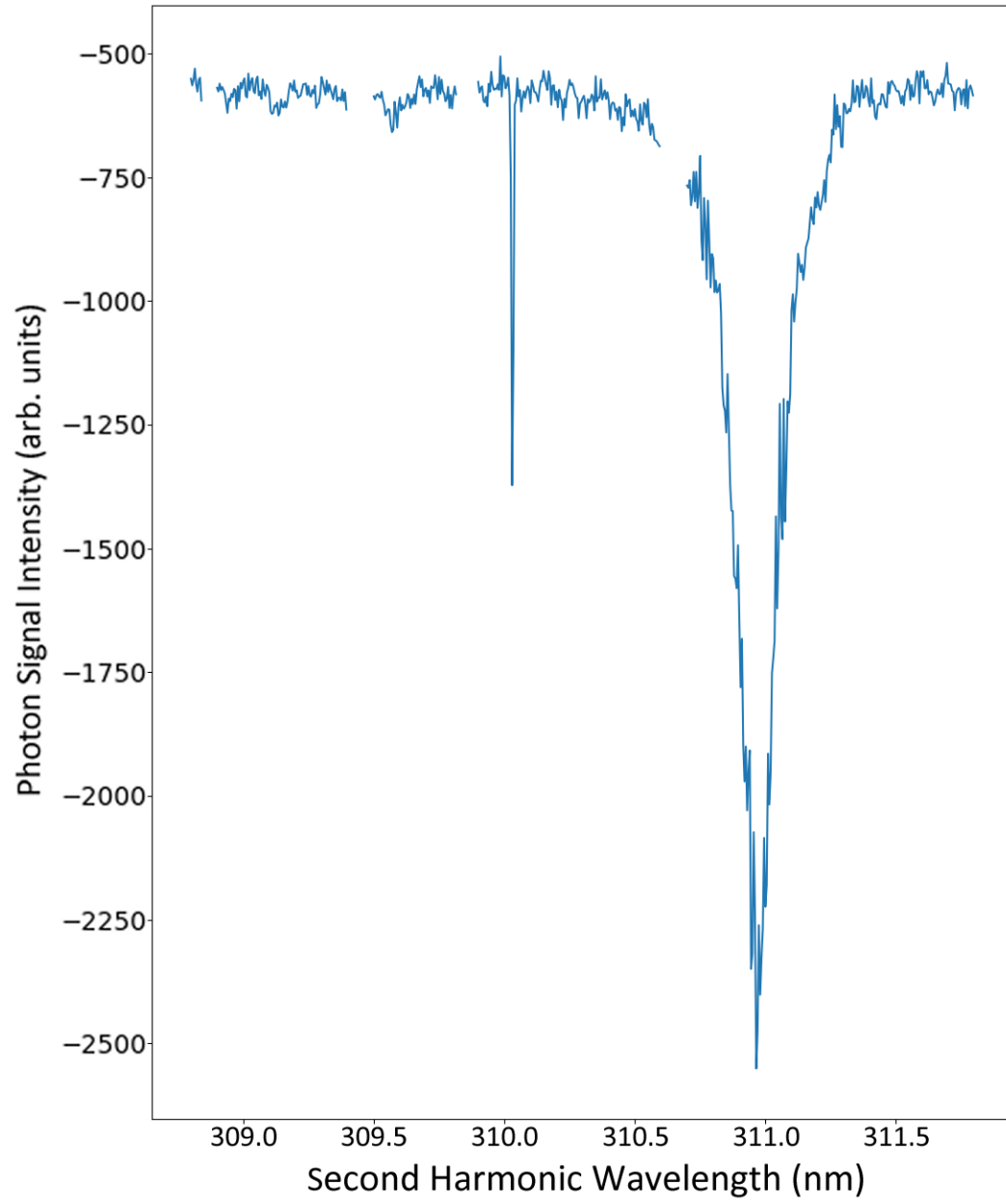


Figure 3.2: Photodetector readings with oxygen.

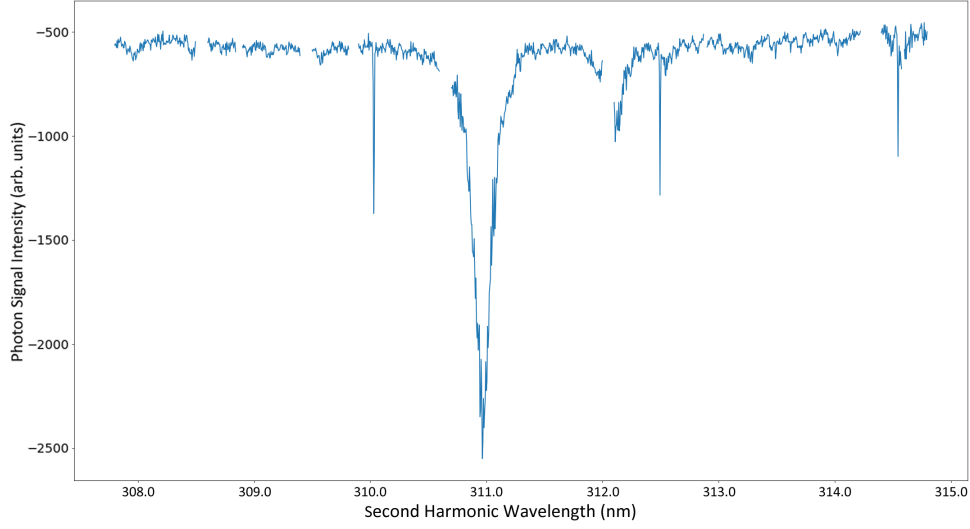


Figure 3.3: Photodetector readings with oxygen over a wider frequency range.

The scan uses the fundamental and second harmonic of the dye laser to identify transitions of both Ta and TaO. Figures 3.2 & 3.1 show the plots obtained with and without O_2 respectively, which are compared with each other to distinguish TaO signals from those of Ta. Unfortunately, the Ta signal seen as the smaller peak in Figure 3.2 wasn't successfully transferred from the oscilloscope to the data acquisition program in Figure 3.1. However, a comparison shows that the large peak clearly corresponds to TaO.

The smaller peaks are found to correspond to Ta transitions at 310.4150 and 312.8772 nm [16], the two larger peaks at 310.8 (621.6) and 314.5 (629.0) nm agree with the v_{00} TaO transitions from the ground to F 10 (16051 cm^{-1}) and E (15880.6 cm^{-1}) states respectively [17], while the third peak at 312.0 (624.0) nm is likely

associated with the v_{11} transition from the ground to F 10 state. This preliminary scan shows good agreement, and the next step is to improve the scan resolution to study the spectrum in more detail.

CHAPTER 4

OUTLOOK

Preliminary scans of Ta and TaO have been successful, although there is plenty of room for improvement. The laser linewidth hasn't been fully optimized, so there may be the possibility of some peaks overlapping with each other. In particular, the degradation of the beam profile in the dye laser has been a persistent issue for the past year, which has recently been partially resolved by renewing the dye. Previously, dye was expected to last longer if it was used less, but the degradation was faster than expected. The remainder of optimizing the linewidth lies in the alignment of the optical components of the dye laser. A camera monitoring the beam profile can be used to initially determine the linewidth of the laser based off of the thickness of the interference fringes from the monitor etalon, but a more qualitative measurement can be obtained by using the program previously used to correct the nonlinearity of the peak distances.

Aside from optimizations, the next step would involve looking for TaO transitions in unexplored frequency ranges. Of particular interest is the 30,000 - 45,000 cm^{-1} range for TaO, in which there aren't many recorded transitions.

Aside from TaO, the apparatus is able to produce other molecular species composed of a metallic and gaseous element, such as ThF. Spectroscopy can likewise be

done on those individual components by using an inert gas mixture for the former and disabling ablation for the latter.

While outside the scope of this study, the apparatus is capable of REMPI with the same setup by adjusting the frequencies of the excitation lasers. Ions (such as TaO^+) produced this way can be further studied by co-trapping an individual ion with an atomic ion, which allows for quantum logic spectroscopy. This technique couples the two ions to each other through the Coulomb interaction, allowing for the cooling and spectroscopy of the molecular ion through the atomic ion, the latter which is much easier to work with.

There are several pathways of study that can be achieved through this apparatus. Therefore it is necessary to properly evaluate its reliability and limitations. Through this study, many considerations have been affirmed, and several others have been reevaluated, such as the lifetime of the dye which determines the quality of the ionization lasers. Through careful planning and revision, the apparatus has been successfully tested and is ready to move onto its next stage.

BIBLIOGRAPHY

- [1] Cairncross, W. B. *et al.* Precision measurement of the electron’s electric dipole moment using trapped molecular ions. *Phys. Rev. Lett.* **119**, 153001 (2017). URL <https://link.aps.org/doi/10.1103/PhysRevLett.119.153001>.
- [2] ACME collaboration. Improved limit on the electric dipole moment of the electron. *Nature* **562**, 355–360 (2018). URL <https://doi.org/10.1038/s41586-018-0599-8>.
- [3] LIOP-TEC GmbH, Radevormwald, North Rhine-Westphalia, Germany. *Tunable Pulsed Dye Laser User Manual* (2012).
- [4] Geary, J. M. Introduction to optical testing. *SPIE Optical Engineering Press TT 15* (1993).
- [5] Sakharov, A. Violation of cp invariance, c asymmetry, and baryon asymmetry of the universe. *Journal of Experimental and Theoretical Physics Letters* **5**, 24–27 (1967).
- [6] Safronova, M. S. *et al.* Search for new physics with atoms and molecules. *Rev. Mod. Phys.* **90**, 025008 (2018). URL <https://link.aps.org/doi/10.1103/RevModPhys.90.025008>.
- [7] Pospelov, M. & Ritz, A. Ckm benchmarks for electron electric dipole moment experiments. *Phys. Rev. D* **89**, 056006 (2014). URL <https://link.aps.org/doi/10.1103/PhysRevD.89.056006>.
- [8] Skripnikov, L. V., Petrov, A. N., Mosyagin, N. S., Titov, A. V. & Flambaum, V. V. Tan molecule as a candidate for the search for a t,p-violating nuclear magnetic quadrupole moment. *Phys. Rev. A* **92**, 012521 (2015). URL <https://link.aps.org/doi/10.1103/PhysRevA.92.012521>.
- [9] Flambaum, V. V., DeMille, D. & Kozlov, M. G. Time-reversal symmetry violation in molecules induced by nuclear magnetic quadrupole moments. *Phys. Rev. Lett.* **113**, 103003 (2014). URL <https://link.aps.org/doi/10.1103/PhysRevLett.113.103003>.
- [10] Fleig, T. TaO⁺ as a candidate molecular ion for searches of physics beyond the standard model. *Phys. Rev. A* **95**, 022504 (2017). URL <https://link.aps.org/doi/10.1103/PhysRevA.95.022504>.

- [11] Sakurai, J. J. & Napolitano, J. *Modern Quantum Mechanics* (Cambridge University Press, New York, NY, USA, 2021), 3rd edn.
- [12] Dunning, F. B. & Hulet, R. G. *Experimental Methods in the Physical Sciences*, vol. 29B (Elsevier Science & Technology, Amsterdam, Netherlands, 1996), 1st edn.
- [13] Spectra-Physics Lasers & Photonics, Mountain View, CA, USA. *Quanta-Ray Lab Series Pulsed Nd:YAG Lasers User's Manual* (2003).
- [14] Nagourney, W. *Quantum Electronics for Atomic Physics* (Oxford University Press, New York, NY, USA, 2010), 1st edn.
- [15] Fowles, G. R. *Introduction to Modern Optics* (Dover Publications, New York, NY, USA, 1975), 2nd edn.
- [16] Kramida, A., Ralchenko, Y., Reader, J. & Team, N. A. *NIST Atomic Spectra Database (ver. 5.9)* (National Institute of Standards and Technology, Gaithersburg, MD, USA).
- [17] Huber, K. P. & Herzberg, G. H. *Constants of Diatomic Molecules in NIST Chemistry WebBook, NIST Standard Reference Database Number 69* (National Institute of Standards and Technology, Gaithersburg, MD, USA).

CURRICULUM VITAE

Timothy Chung
timothyychung@gmail.com

EDUCATION

GRADUATE:

M.Sc. in Physics at University of Nevada, Las Vegas (UNLV) *Current*
Research: Design and construction of an apparatus for high-resolution spectroscopy, with a search for known transitions of TaO to test the apparatus.

UNDERGRADUATE:

B.A. in Physics at Occidental College *July 2018*
Minors: Mathematics
Research: Thermal expansion and magnetostriction of ytterbium nickel borocarbide near T_c .

RESEARCH INTERESTS

My area of interest is in condensed matter physics, specifically in the applications of superconductors. Undergraduate research developed my interest in superconductors, where I measured the thermal expansion and magnetostriction of superconducting rare earth nickel borocarbides in a dilatometer to study their superconducting phase transitions. Graduate research allowed me to explore the field of AMO physics, where I learned more about the different techniques in spectroscopy as I built an apparatus for high-resolution spectroscopy. I seek to return to my area of interest and make use of what I learned in this study by working on a quantum transducer which bridges the gap between ion trap and superconducting circuit quantum computers.

EXPERIENCE

Graduate Assistant (UNLV) *August 2020 - present*
- Instruction of intro-level physics labs.

International Symposium on Molecular Spectroscopy *June 24, 2021*
- Presented poster: "*TaO+ Spectroscopy to Facilitate Exploring New Physics Beyond the Standard Model*"

Tutor at Office of Special Services at Los Angeles City College *August 2011 - May 2012*
- Tutoring for students with learning disabilities.

ACHIEVEMENTS

Graduate Assistantship (UNLV) *Fall 2020 - Spring 2022*